

Jekyll & Hyde: quiescence and extreme obscuration in a pair of massive galaxies 1.5 Gyr after the Big Bang

C. Schreiber¹, I. Labbé¹, K. Glazebrook², G. Bekiaris^{2,3}, C. Papovich⁴, T. Costa¹, D. Elbaz⁵, G. G. Kacprzak²,
T. Nanayakkara¹, P. Oesch⁶, M. Pannella⁷, L. Spitler^{8,9,10}, C. Straatman¹¹, K.-V. Tran^{3,12}, and T. Wang^{13,14}

¹ Leiden Observatory, Leiden University, NL-2300 RA Leiden, The Netherlands
e-mail: cschreib@strw.leidenuniv.nl

² Centre for Astrophysics and Supercomputing, Swinburne University of Technology, Hawthorn, VIC 3122, Australia

³ Australia Telescope National Facility, CSIRO Astronomy and Space Science, PO Box 76, Epping, NSW 1710, Australia

⁴ George P. and Cynthia W. Mitchell Institute for Fundamental Physics and Astronomy, Department of Physics and Astronomy, Texas A&M University, College Station, TX 77843, USA

⁵ AIM-Paris-Saclay, CEA/DSM/Irfu – CNRS – Université Paris Diderot, CEA-Saclay, pt courrier 131, 91191 Gif-sur-Yvette, France

⁶ Observatoire de Genève, 1290 Versoix, Switzerland

⁷ Faculty of Physics, Ludwig-Maximilians Universität, Scheinerstr. 1, 81679 Munich, Germany

⁸ Research Centre for Astronomy, Astrophysics & Astrophotonics, Macquarie University, Sydney, NSW 2109, Australia

⁹ Department of Physics & Astronomy, Macquarie University, Sydney, NSW 2109, Australia

¹⁰ Australian Astronomical Observatory, 105 Delhi Rd., Sydney NSW 2113, Australia

¹¹ Max-Planck Institut für Astronomie, Königstuhl 17, D-69117, Heidelberg, Germany

¹² School of Physics, University of New South Wales, Sydney, NSW 2052, Australia

¹³ Institute of Astronomy, The University of Tokyo, Osawa, Mitaka, Tokyo 181-0015, Japan

¹⁴ National Astronomical Observatory of Japan, Mitaka, Tokyo 181-8588, Japan

Received 08 September 2017; accepted 07 December 2017

ABSTRACT

We obtained ALMA spectroscopy and deep imaging to investigate the origin of the unexpected sub-millimeter emission toward the most distant quiescent galaxy known to date, ZF-COSMOS-20115 at $z = 3.717$. We show here that this sub-millimeter emission is produced by another massive ($M_* \sim 10^{11} M_\odot$), compact ($r_{1/2} = 0.67 \pm 0.14$ kpc) and extremely obscured galaxy ($A_V \sim 3.5$), located only $0.43''$ (3.1 kpc) away from the quiescent galaxy. We dub the quiescent and dusty galaxies *Jekyll* and *Hyde*, respectively. No dust emission is detected at the location of the quiescent galaxy, implying $\text{SFR} < 13 M_\odot/\text{yr}$ which is the most stringent upper limit ever obtained for a quiescent galaxy at these redshifts. The two sources are spectroscopically confirmed to lie at the same redshift thanks to the detection of $[\text{C II}]_{158}$ in *Hyde* ($z = 3.709$), which provides one of the few robust redshifts for a highly-obscured “H-dropout” galaxy ($H - [4.5] = 5.1 \pm 0.8$). The $[\text{C II}]$ line shows a clear rotating-disk velocity profile which is blueshifted compared to the Balmer lines of *Jekyll* by 549 ± 60 km/s, demonstrating that it is produced by another galaxy. Careful de-blending of the *Spitzer* imaging confirms the existence of this new massive galaxy, and its non-detection in the *Hubble* images requires extremely red colors and strong attenuation by dust. Full modeling of the UV-to-far-IR emission of both galaxies shows that *Jekyll* has fully quenched at least 200 Myr prior to observation and still presents a challenge for models, while *Hyde* only harbors moderate star-formation with $\text{SFR} \lesssim 120 M_\odot/\text{yr}$, and is located at least a factor 1.4 below the $z \sim 4$ main sequence. *Hyde* could also have stopped forming stars less than 200 Myr before being observed; this interpretation is also suggested by its compactness comparable to that of $z \sim 4$ quiescent galaxies and its low $[\text{C II}]/\text{FIR}$ ratio, but significant on-going star-formation cannot be ruled out. Lastly, we find that despite its moderate SFR, *Hyde* hosts a dense reservoir of gas comparable to that of the most extreme starbursts. This suggests that whatever mechanism has stopped or reduced its star-formation must have done so without expelling the gas outside of the galaxy. Because of their surprisingly similar mass, compactness, environment and star-formation history, we argue that *Jekyll* and *Hyde* can be seen as two stages of the same quenching process, and provide a unique laboratory to study this poorly understood phenomenon.

Key words. Galaxies: evolution – galaxies: high-redshift – galaxies: kinematics and dynamics – galaxies: star formation – galaxies: stellar content – sub-millimeter: galaxies

1. Introduction

In the local Universe, more than half of the stellar mass is found in quiescent galaxies (e.g., Bell et al. 2003) with current star-formation rates (SFRs) only $\lesssim 1\%$ of their past average (e.g., Pasquali et al. 2006). Unlike star-forming galaxies, which are predominantly rotating disks, quiescent galaxies have spheroidal shapes, very dense stellar cores, and dispersion-dominated kinematics. They contain very little atomic and molecular gas (e.g., Combes et al. 2007; Saintonge et al. 2016), and most of their

gas is instead ionized (e.g., Annibali et al. 2010). These galaxies also frequently possess an active galactic nucleus (AGN; e.g., Lee et al. 2010), signpost of accretion of matter onto a central super-massive black hole. Lastly, they tend to be much rarer at low stellar masses (e.g., Baldry et al. 2004), and more abundant in dense environments (e.g., Peng et al. 2010).

The formation channel of such galaxies remains uncertain. A number of mechanisms have been proposed to stop (i.e., “quench”) or reduce star-formation, and all effectively act to de-

plete the cold gas reservoirs. This can be achieved by a) removing cold gas from the galaxy through outflows, b) pressurizing the gas and preventing it from collapsing, c) stopping the supply of infalling gas until star-formation exhausts the available reserves, or d) any combination of these. The underlying physical processes could be various, including feedback from stars or an AGN, injection of kinetic energy from infalling gas, stabilization of a gas disk by a dense stellar core, or tidal interactions with massive neighboring galaxies (e.g., Silk & Rees 1998; Birnboim & Dekel 2003; Croton et al. 2006; Gabor & Davé 2012; Martig et al. 2009; Förster Schreiber et al. 2014; Genzel et al. 2014; Peng et al. 2015). While there is evidence that each of these phenomena does (or can) happen in at least some galaxies, it still remains to be determined which of them actually plays a significant role in producing the observed population of quiescent galaxies.

At higher redshifts, where spectroscopy is scarce and more expensive, selecting quiescent galaxies is challenging. Yet this has proven to be a powerful tool to constrain their formation mechanism and the overall process driving the growth of galaxies in general (e.g., Peng et al. 2010). In the absence of spectroscopy, selection criteria based on red broad-band colors have been designed, preferably with two colors to break the age-dust degeneracy (Franx et al. 2003; Labbé et al. 2007; Williams et al. 2009; Arnouts et al. 2013). Using such methods, it was found that quiescent galaxies were less numerous in the past (e.g., Labbé et al. 2007; Muzzin et al. 2013; Ilbert et al. 2013; Tomczak et al. 2014), consistent with the fact that this population has been slowly building up with time. Surprisingly, quiescent and massive galaxies are still found up to very high redshifts (Glazebrook et al. 2004; Straatman et al. 2014), implying that star-formation may be more rapid and quenching more efficient than envisioned by most models.

Yet, spectroscopic confirmation of their redshifts and quiescence is required to draw firm conclusions (e.g., Kriek et al. 2009; Gobat et al. 2012). In Glazebrook et al. (2017) we reported the spectroscopic identification of the most distant quiescent galaxy known to date, ZF-COSMOS-20115, at $z = 3.717$. The galaxy was first identified in Straatman et al. (2014) thanks to its strong Balmer break, and its redshift was subsequently confirmed using deep Balmer absorption lines, a clear indicator of a recent shutdown of star-formation. This allowed us to precisely trace back the star-formation history of this galaxy, which we estimated must have stopped at $z > 5$ and required a large peak SFR $\sim 1000 M_{\odot}/\text{yr}$. While some models can accommodate quenched galaxies this early in the history of the Universe (e.g., Rong et al. 2017; Qin et al. 2017), none is able to produce them in numbers large enough to match observations.

Despite its apparently quenched star-formation history, faint sub-millimeter emission was detected toward the galaxy ZF-COSMOS-20115 with ALMA (Schreiber et al. 2017b), with a spatial offset of $0.4 \pm 0.1''$. This suggested that star-formation might still be on-going in an obscured region of the galaxy, and would thus have escaped detection at shorter wavelengths. As discussed in Glazebrook et al. (2017), this emission is faint enough that the corresponding SFR, even if indeed associated with the quiescent galaxy, would only account for up to 15% of the total observed stellar mass over the last 200 Myr. Therefore, regardless of the sub-millimeter emission, the bulk of the mass in this galaxy had necessarily formed earlier on. But the questions remained of whether the galaxy has actually quenched, and what is truly powering the sub-millimeter emission (see also Simpson et al. 2017).

To answer these questions, we have obtained deeper and higher-resolution continuum imaging at $744 \mu\text{m}$ with ALMA, in a spectral window centered on the expected frequency of $[\text{C II}]_{158}$ at $z = 3.717$. The present paper discusses these new observations and what they reveal about the true nature of this system. In the following, we refer to the quiescent galaxy as “*Jekyll*” and the sub-millimeter source as “*Hyde*”.

The flow of the paper goes as follows. In section 2 we describe the dust and $[\text{C II}]$ data we used in this paper, and how we modeled them. The relative astrometry between ALMA and *Hubble* is quantified in section 2.2, and the flux extraction is detailed in section 2.3. The dust emission modeling and results are described in section 2.4, while the modeling of the kinematics of the $[\text{C II}]$ line is addressed in section 2.5. We then study the stellar emission of *Jekyll* and *Hyde* in section 3, starting from the UV to near-IR photometry in section 3.1, following by a description of the spectral modeling in section 3.2 and a description of the results in section 3.3. In section 4 we put together and discuss these observations. Section 4.1 addresses the non-detection of the dust continuum in *Jekyll* and its quiescent nature, and section 4.2 demonstrates that *Hyde* is indeed a separate galaxy. We then study evidence for a recent or imminent quenching in *Hyde*, based on its compactness in section 4.3 and low $[\text{C II}]$ luminosity in section 4.4. The efficiency of star-formation and possible quenching processes are discussed in section 4.5. Lastly, section 4.6 speculates on how *Hyde* can be viewed as a younger version of *Jekyll*, and what links can be drawn between the two galaxies. We then summarize our conclusions in section 5.

In the following, we assumed a ΛCDM cosmology with $H_0 = 70 \text{ km s}^{-1} \text{ Mpc}^{-1}$, $\Omega_M = 0.3$, $\Omega_{\Lambda} = 0.7$ and a Chabrier (2003) initial mass function (IMF), to derive both star-formation rates and stellar masses. All magnitudes are quoted in the AB system, such that $M_{\text{AB}} = 23.9 - 2.5 \log_{10}(S_{\nu} [\mu\text{Jy}])$.

2. Dust continuum and $[\text{C II}]$ emission

The first observations toward this system with ALMA were obtained at 338 GHz ($888 \mu\text{m}$) in band 7, targeting *Jekyll* as part of a larger program (2013.1.01292.S, PI: Leiton) observing massive $z \sim 4$ galaxies (Schreiber et al. 2017b). The on-source observing time was only 1.5 minutes, and the resulting noise level reached 0.25 mJy (1σ) with a beam of full width at half maximum of $1.1 \times 0.7''$. Nevertheless, a source was detected at 5σ significance with a flux of $1.52 \pm 0.25 \text{ mJy}$, slightly offset from the position of *Jekyll* ($0.5 \pm 0.1''$). This detection was already discussed in our previous work where we introduced *Jekyll* (Glazebrook et al. 2017). At the time, the spatial offset was already deemed significant, although the limited signal-to-noise ratio of the ALMA source as well as the relatively wide beam were such that its interpretation was difficult.

Once the ALMA emission was discovered, we proposed to re-observe this system with better sensitivities and angular resolution, and sought to detect the $[\text{C II}]$ line to confirm the redshift. These observations are described in the next sections, together with the flux extraction and modeling procedure (both for the ALMA data and ancillary imaging from *Spitzer* and *Herschel*). All our results are summarized in Table 1.

2.1. Overview of ALMA observations and flux extraction

The new ALMA data were obtained in band 8 with a single spectral tuning at 403 GHz ($744 \mu\text{m}$), and were delivered in early 2017 as part of the Director’s Discretionary Time (DDT) program 2015.A.00026.S. The on-source observing time was 1.2

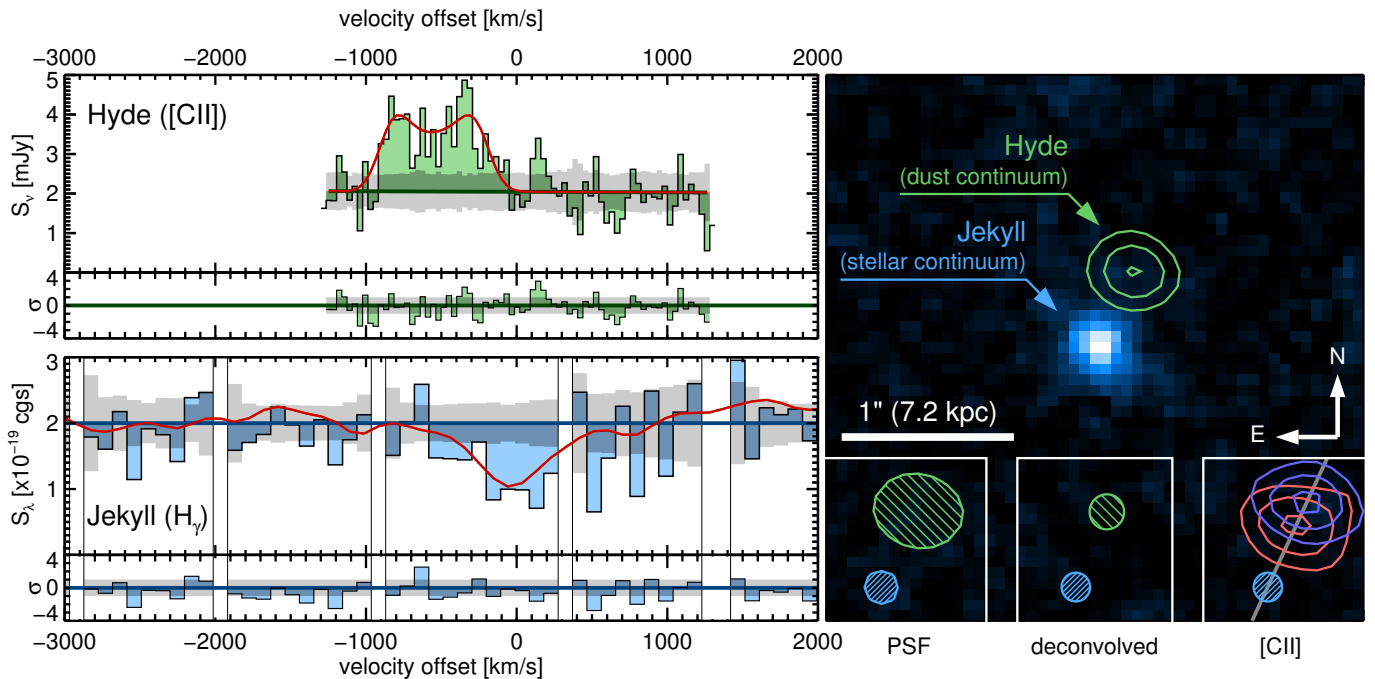


Fig. 1. Spectra and imaging of *Jekyll & Hyde*. **Top left:** ALMA spectrum of *Hyde*. **Bottom left:** MOSFIRE spectrum of *Jekyll* (binned to 6.5 \AA resolution). The two spectra are shown on the same velocity scale. The emission above and below the continuum level is shaded to emphasize the lines. The gray shaded area in the background is the 1σ flux uncertainty. We show the models best fitting these spectra with red lines. At the bottom of each plot we give the normalized model residual σ , i.e., the difference between observed and modeled flux divided by the uncertainty. **Right:** image of the *Jekyll & Hyde* system. The background image (blue tones; false colors) is the near-IR *H*-band emission (as observed by *Hubble*); the bright source at the center is *Jekyll*. We overlay the ALMA $740 \mu\text{m}$ continuum emission with green contours (the most extended contour corresponds half of the peak emission); the source detected here is *Hyde*. The full width at half maximum of the *Hubble* and ALMA point spread functions are given on the bottom left corner, followed to the right by the deconvolved profiles of the two galaxies (half-light area). Lastly, the inset on the bottom right corner shows the position of the two velocity components of *Hyde* with respect to *Jekyll* (the blue contours correspond to the most blueshifted component), and a gray line connects the two galaxies.

hours, with a beam size of $0.52 \times 0.42''$ (natural weighting), about a factor of two smaller than the first observations. The pointing was centered on the *Hubble Space Telescope* (*HST*) position of *Jekyll*: $\alpha = 150.06146^\circ$, $\delta = 2.378683^\circ$.

We generated two spectral cubes in CASA corresponding to two pairs of spectral windows of disjoint frequency range, the first centered on the expected frequency of the $[\text{C II}]$ line (401.2 to 404.7 GHz), and the second at higher frequencies which only measure the continuum level (413.0 to 416.5 GHz). We did not perform any cleaning on these cubes, and thus used the dirty images throughout this analysis with the dirty beam as point-spread function. We binned the flux of every three frequency channels to eliminate correlated noise between nearby channels, and determined the noise level in each channel using the RMS of the pixels away from the source (without applying the primary-beam correction). We found that the frequencies 402.4 and 414.3 GHz are affected by known atmospheric lines which increase the noise by a factor of two, the former can be seen on Fig. 1 (top-left) at $+400 \text{ km/s}$.

To extract the continuum and line flux of the target, we proceeded as follows. We first created a “continuum+line” image by averaging all spectral channels together, and located the peak position of the emission. A bright source was found, with a peak flux of $2.36 \pm 0.06 \text{ mJy}$, and clearly offset from the position of the quiescent galaxy by about $0.5''$. The accuracy of the astrometry is demonstrated in section 2.2, and the offset is discussed further in section 2.3. We then extracted a spectrum, shown in Fig. 1 (top-left), at this peak position and found a line close to the ex-

pected frequency of $[\text{C II}]$ at $z \sim 3.7$ (throughout this paper, we assumed a vacuum rest frequency $\nu_{[\text{C II}]\text{rest}} = 1900.5369 \text{ GHz}$, which known with an excellent accuracy of $\Delta\nu = 1.3 \text{ MHz}$; Cooksey et al. 1986). The line is relatively broad and its kinematics resembles more a “double horn”, typical of rotating disks, than a single Gaussian.

We created a continuum image by masking the spectral channels containing the $[\text{C II}]$ emission. From this image we extracted the size and total continuum flux of the source, as described in section 2.3. This flux and the ancillary *Herschel* and SCUBA-2 photometry is modeled in section 2.4. We then subtracted the continuum map from the spectral cube and fit the $[\text{C II}]$ emission with a rotating disk model described in section 2.5. This model was used to determine the spatial extent, total flux, and kinematics of the $[\text{C II}]$ emission.

2.2. ALMA astrometry

Given the $S/N = 40$ of the detection in the new ALMA image, the position of the dust emission is known with an uncertainty of $0.01''$. Since the *Hubble* imaging of *Jekyll* also provides a high S/N detection and shows that *Jekyll* is very compact ($r_{1/2} = 0.07 \pm 0.02''$; Straatman et al. 2015), the two sources are undoubtedly offset. However, since *Jekyll* and *Hyde* are each detected by a different instrument, it is possible that either image is affected by a systematic astrometric issue which could spuriously generate such an offset. For example Rujopakarn et al. (2016) and Dunlop et al. (2017) have revealed that the *Hubble*

imaging in the GOODS–South field was affected by a systematic astrometry shift of about $0.26''$, when compared to images from ALMA, VLA and 2MASS. The same study also showed that VLA and ALMA positions match within $0.04''$.

The two galaxies discussed in the present paper are located in the COSMOS field. Here, all the UV-to-NIR images (including that from *Hubble*) are tied to a common astrometric frame defined by the CFHT i^* -band image, which itself is ultimately anchored to the radio image from the VLA (Koekemoer et al. 2007). Since both ALMA and VLA have been shown to provide consistent absolute astrometry, we do not expect such large offsets to exist in the COSMOS field. A comparison of the *Hubble* astrometry against Pan-STARRS suggests indeed that no large offset exists in this field (M. Dickinson, private communication).

To confirm this, we have retrieved from the ALMA archive¹ the images of sub-millimeter galaxies in the COSMOS field, observed in bands 6 and 7, and which have a clear counterpart in the VISTA K_s image within a $1.5''$ radius. We chose the K_s -band image as a reference instead of the *HST* band since it provides the best S/N for this sub-millimeter sample, and also because it covers the entire COSMOS field. Since both the K_s and *HST* images are tied to the same astrometric reference (see above), the results we discuss below also apply to the *HST* imaging.

For each source, we estimated the uncertainty in the ALMA and VISTA centroids, which depend on the signal-to-noise ratio (S/N) of the source and the size of the beam or point spread function (σ_{beam}) as $\Delta p_{N,X} = \sqrt{2} \sigma_{\text{beam}} / (S/N)$. Defining $\Delta p_N^2 = \Delta p_{N,\text{ALMA}}^2 + \Delta p_{N,\text{VISTA}}^2$, we then excluded sources with $\Delta p_N > 0.15''$ to only consider the well-measured centroids. To avoid blending issues, we excluded from this sample the sources detected as more than one component in the K_s image or with a neighbor within $2''$. To avoid physical offsets caused by patchy obscuration, we also excluded galaxies with a detection on the Subaru i image significantly offset from the K_s centroid. This adds up to a sample of 71 galaxies. For each source, we measured the position of both the ALMA and K_s sources as the flux weighted average of the x and y coordinates and computed the positional offset between the two.

The resulting absolute offsets are displayed in Fig. 2. We found an average of $\Delta\alpha = +0.068 \pm 0.012''$ and $\Delta\delta = -0.031 \pm 0.013''$ (ALMA – VISTA), which is confined to less than $0.1''$ but nevertheless significant (see also Smolčić et al. 2017 where a similar offset was reported). However, these numbers only apply to the COSMOS field as a whole (our sample spans $1.2^\circ \times 1.1^\circ$); systematic offsets may vary spatially, but average out when computed over the entire field area. To explore this possibility, we selected only the galaxies that lie within $5'$ of our objects, reducing the sample to six galaxies. In this smaller but more local sample, we found averages of $\Delta\alpha = +0.11 \pm 0.03''$ and $\Delta\delta = +0.04 \pm 0.04''$, which are consistent with the previous values thus imply no significant variation across the field. For all the following, we therefore assumed the global offset derived above and brought the ALMA positions back into the same astrometric reference as the optical-NIR images.

After subtracting this small systematic offset, the largest offset we observed in the full sample of 71 galaxies was $0.33''$, and $0.20''$ in the smaller sample of six galaxies. These values are both lower than the $\sim 0.5''$ offset we observed between *Jekyll* and *Hyde* and suggest that the latter being offset by chance is unlikely. We quantify this in the next paragraph.

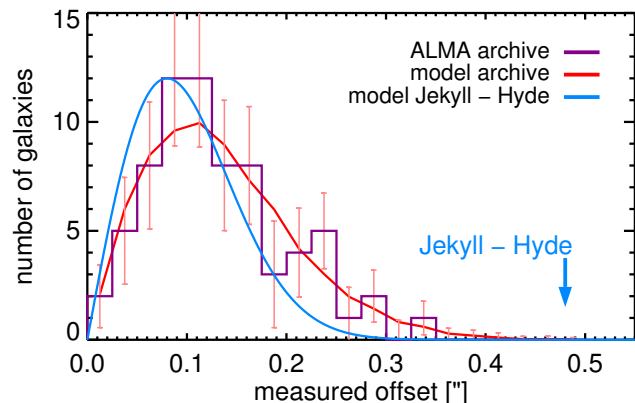


Fig. 2. Distribution of observed positional offsets between ALMA and VISTA in the COSMOS field. The purple histogram shows the observed distribution for 76 galaxies selected from the ALMA archive, and the red line is the best-fit model (including telescope pointing accuracy and uncertainty in the centroid determination on noisy images). Error bars show counting uncertainties derived assuming Poisson statistics from the best-fit model. The blue arrow shows the offset observed between *Jekyll* and *Hyde*, and the blue line is the expected offset distribution given the S/N and PSF width of the two galaxies on their respective images.

To determine the random astrometric registration errors between ALMA and VISTA, we modeled the observed offsets using two sources of offsets (per coordinate). On the one hand, we considered random offsets caused by noise in the ALMA and VISTA images, the amplitude of which are given by Δp_N as described above. On the other hand, we considered the combined pointing accuracy of ALMA and VISTA Δp_T , which we assumed is a constant value identical for both coordinates. The total uncertainty on a coordinate of the source i is then $\Delta p(i)^2 = \Delta p_N(i)^2 + \Delta p_T^2$. Varying Δp_T on a grid from 0 to $0.5''$, we generated 200 Monte Carlo simulations of the sample and compared the simulated offset distribution to the observed one using a Kolmogorov-Smirnov test. We found $\Delta p_T = 0.080 \pm 0.009''$, and display the best-fit model in Fig. 2. The probability of observing a given offset by chance is then governed by a Rayleigh distribution of scale parameter $\Delta p(i)$. In the case of *Jekyll* and *Hyde*, the S/N in both VISTA and ALMA is high such that $\Delta p_N = 0.02'' \ll \Delta p_T$. This implies the probability of observing an offset of $\geq 0.4''$ by chance is only 10^{-4} (see Fig. 2), and even less if we consider that the offset is observed independently in both band 7 and band 8 images. The observed offset is therefore real.

2.3. Fluxes and spatial profiles

We used `imfit`² v1.5 (Erwin 2015) to model the dust continuum emission, assuming an exponential disk profile (Hodge et al. 2016) and Gaussian noise. Since we model the dirty image directly, the correct point-spread function to use in the modeling is the dirty beam. However since this beam has a zero integral, one should not re-normalize it at any stage of the modeling. We therefore had to disable the re-normalization of the PSF in `imfit` using the `--no-normalize` flag. We cross-checked our results by modeling the continuum emission in line-free channels using

¹ Projects 2013.1.00034.S, 2013.1.00118.S, 2013.1.00151.S, 2015.1.00137.S, 2015.1.00379.S and 2015.1.01074.S.

² <https://github.com/perwin/imfit>

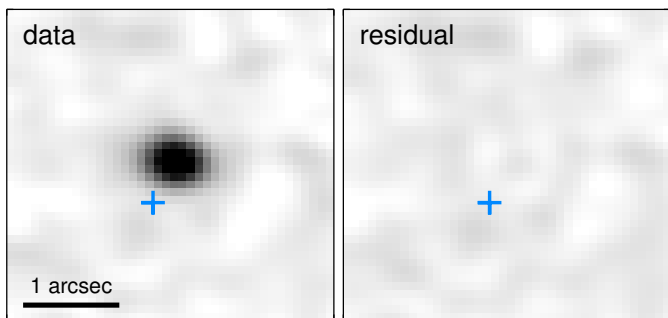


Fig. 3. ALMA $744\ \mu\text{m}$ continuum emission (left) and residual (right) after subtracting the best-fit exponential disk model with *imfit*. The centroid of the *HST* emission of *Jekyll* is indicated with a blue cross. The beam FWHM is $0.52 \times 0.42''$.

both *uvmodel*fit and *uvmultifit* (Martí-Vidal et al. 2014), which both analyze the emission directly in the (u, v) plane rather than on reconstructed images, and found similar results.

To compute uncertainties in the model parameters, we ran *imfit* on simulated data sets with the same noise as the observed data (i.e., a white Gaussian noise map convolved with the dirty beam and re-normalized to the RMS of the observed image), where we artificially injected a source with the same size and flux as our best-fit model. The uncertainties were then determined from the standard deviation of the best fits among all simulated data sets.

The ALMA emission and residual are shown in Fig. 3. We measured for *Hyde* a total continuum flux of $S_{744\ \mu\text{m}} = 2.31 \pm 0.14\ \text{mJy}$, offset from *Jekyll* by $\Delta\alpha = -0.132 \pm 0.017''$ and $\Delta\delta = +0.405 \pm 0.015''$, which is consistent with the offset previously measured in the shallower data. This corresponds to a projected distance of $0.426 \pm 0.015''$, i.e., $3.05 \pm 0.11\ \text{kpc}$. We showed in section 2.2 that this offset is highly significant: the dust emission must therefore originate from another object, *Hyde*. This source is marginally resolved, with a half-light radius of $0.10 \pm 0.02''$ (i.e., the source is about half the size of the dirty beam). At $z = 3.7$, this corresponds to $0.67 \pm 0.14\ \text{kpc}$.

No significant continuum emission is detected at the location of *Jekyll* ($0.09 \pm 0.06\ \text{mJy}$, assuming a point source, and accounting for de-blending and astrometry uncertainty using the procedure described in section 3.1). As illustrated in Fig. 1 (right), the projected distance between *Jekyll* and *Hyde* is much larger than their respective half-light radii (by a factor ~ 5), therefore the two galaxies do not overlap and form two separate systems.

The far-IR photometry toward the *Jekyll + Hyde* system was re-extracted from *Spitzer* MIPS and *Herschel* imaging following a method standard to deep fields (Elbaz et al. 2011), and briefly summarized below. Given the large beam sizes, it is impossible to de-blend *Jekyll* and *Hyde* on these images. Motivated by the fact that *Jekyll* is at least ~ 20 times fainter than *Hyde* on the $744\ \mu\text{m}$ image, we assumed that the entirety of the MIPS and *Herschel* fluxes is produced by *Hyde*.

To account for the poor angular resolution of far-IR images, we modeled all sources in the ancillary images within a $5' \times 5'$ region centered on the system. The 24 to $160\ \mu\text{m}$ images were modeled with point-like sources at the position of *Spitzer* IRAC-detected galaxies. The 250 to $500\ \mu\text{m}$ images were modeled similarly, using positions of *Spitzer* MIPS-detected galaxies. However since this provided a too high density of prior positions, we performed a second pass where MIPS priors with $250\ \mu\text{m}$ flux

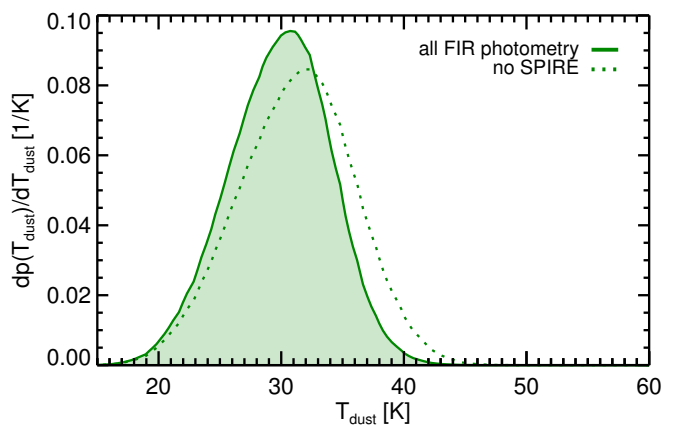


Fig. 4. Probability distribution of the dust temperature (T_{dust}) for *Hyde*. This was derived from the χ^2 of a grid of T_{dust} values tested against the observed photometry. The solid line shows the distribution using all the FIR photometry, and the dotted line shows how the distribution would have changed if we had not used the *Herschel* SPIRE photometry.

less than 3 mJy or negative $500\ \mu\text{m}$ were discarded. *Hyde* was always kept in the prior list. The SCUBA2 $450\ \mu\text{m}$ flux was taken from Simpson et al. (2017) assuming no significant contamination by neighboring sources.

2.4. Far-IR photometry and modeling

We modeled the 24– $890\ \mu\text{m}$ photometry with the simple dust model presented in Schreiber et al. (2017a), and here we briefly recall its main features. This model has three varying parameters: the dust temperature (T_{dust}), the infrared luminosity (L_{IR} , integrated from 8 to $1000\ \mu\text{m}$) and the $8\ \mu\text{m}$ luminosity (L_8). These templates are designed to describe the far-IR SED of star-forming galaxies with the best possible accuracy given this small number of free parameters. They are built from first principles using the dust model of Galliano et al. (2011), and therefore a dust mass (M_{dust}) is also associated to each template in the library. Compared to simpler gray-body models, these templates can accurately describe the emission at wavelengths shorter than the peak of the dust emission.

In the present case, since our data did not constrain the rest-frame $8\ \mu\text{m}$ emission, we fixed $L_{\text{IR}}/L_8 = 8$, which is the value observed for massive star-forming galaxies at $z \sim 2$ (Reddy et al. 2012; Schreiber et al. 2017a). The fit therefore had four degrees of freedom. Before starting the fit, we subtracted from the observed $24\ \mu\text{m}$ flux the estimated contribution from stellar continuum ($3.5\ \mu\text{Jy}$), which we extrapolated from the best-fitting stellar continuum model (section 3.2). Varying the dust temperature, we adjusted the infrared luminosity to best fit the observed data, and chose as best fit the dust temperature leading to the smallest reduced χ^2 . Uncertainties on all parameters were then computed by randomly perturbing the photometry within the error bars and re-doing the fit 5000 times.

The resulting photometry is shown in Fig. 9 (left) along with our best model. We found a dust temperature of $T_{\text{dust}} = 31^{+3}_{-4}\ \text{K}$ and a luminosity $L_{\text{IR}} = 1.1^{+0.4}_{-0.3} \times 10^{12}\ L_{\odot}$ (error bars include the uncertainty on T_{dust}) which is similar to that obtained by Simpson et al. (2017). This corresponds to $\text{SFR}_{\text{IR}} = 110^{+43}_{-33}\ M_{\odot}/\text{yr}$ using the Kennicutt (1998) conversion, adapted to the Chabrier IMF following Madau & Dickinson (2014). The dust mass is

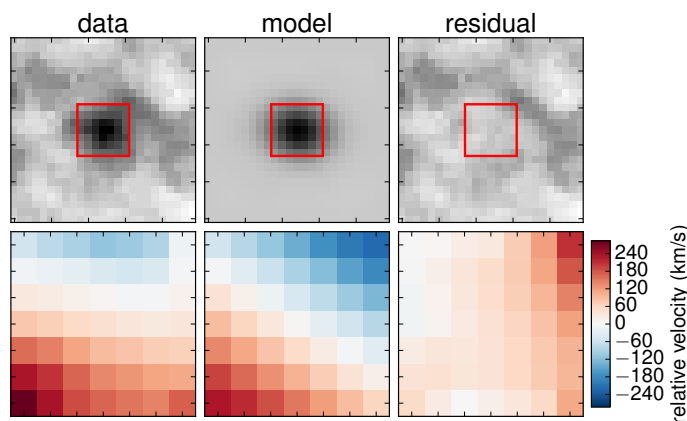


Fig. 5. Result of the modeling of the [C II] line emission with a rotating disk model. The first row shows the spectrally-integrated line intensity map, and the second row is the velocity field in the central region (indicated with a red box in the first row, $0.6'' \times 0.6''$). The beam FWHM is $0.52 \times 0.42''$.

$M_{\text{dust}} = 3.2_{-1.0}^{+2.2} \times 10^8 M_{\odot}$, and is less well constrained than L_{IR} owing to the uncertainty on the dust temperature; the coverage of the dust SED at high and low frequency would need to be improved.

Similar values of $L_{\text{IR}} = 1.4 \times 10^{12} L_{\odot}$ and $\text{SFR}_{\text{IR}} = 140 M_{\odot}/\text{yr}$ were obtained by simply rescaling the SED of the $z = 4.05$ starburst GN20 (Tan et al. 2014), which has a similar dust temperature. In fact, significantly hotter temperatures were ruled out by the non-detections in all *Herschel* bands and the low SCUBA2 $450 \mu\text{m}$ flux, see Fig. 4. For example, assuming $T_{\text{dust}} = 40$ K would have resulted in a combined 2.7σ tension with the observed photometry. Excluding the SPIRE fluxes, which are notoriously difficult to measure, we obtained a similar $T_{\text{dust}} = 32_{-5}^{+4}$ K.

Given that *Jekyll* is not detected in any FIR image, we had to make an assumption on its dust temperature before interpreting its absence on the deep band 8 image. Rather than arbitrarily picking one temperature, we assumed a range of temperatures to obtain more conservative error bars. We considered T_{dust} ranging from 20 K (as observed in $z = 2$ quiescent galaxies; Gobat et al. 2017) to 35 K (the upper limit for *Hyde*) with a uniform probability distribution. With this assumption, the non-detection of *Jekyll* in the band 8 image translates into $L_{\text{IR}} = 3.6_{-2.4}^{+3.1} \times 10^{10} L_{\odot}$, or a 3σ upper limit of $\text{SFR}_{\text{IR}} < 13 M_{\odot}/\text{yr}$. This is the strongest upper limit ever obtained for a single quiescent galaxy at these redshifts (Straatman et al. 2014), and is consistent with its quiescent nature derived from the SED modeling, which we revisit in section 3.3. We note that even if we had assumed a high temperature of $T_{\text{dust}} = 40$ K, which is substantially hotter than *Hyde*, the limits on L_{IR} and SFR_{IR} would still be low: $L_{\text{IR}} = (1.0 \pm 0.7) \times 10^{11} L_{\odot}$ and $\text{SFR}_{\text{IR}} < 31 M_{\odot}/\text{yr}$ (3σ). Yet we consider such high temperatures unlikely; as we demonstrate later in section 3.3, with only $A_V = 0.2\text{--}0.5$ mag the large stellar mass of *Jekyll* is enough to reach $L_{\text{IR}} \sim 10^{11} L_{\odot}$ without on-going star-formation (heating the dust with intermediate-age stars). This leaves little room for dust-obscured star-formation, in which case the dust must be cooler than typically observed in star-forming galaxies (e.g., Gobat et al. 2017).

2.5. Rotating disk model

Since the velocity profile of the [C II] line shows a double-peaked structure, we modeled the continuum-subtracted spectral cube with an inclined thin disk model using GBKFIT³ (Bekiaris et al. 2016). We fixed the centroid of the disk to that of the dust continuum, and varied the scale length ($h = 10^{-5}$ to 3 kpc), the inclination ($i = 5$ to 85°), the position angle (PA = -90 to 90°), the central surface brightness ($I_0 = 0.02$ to 22 mJy/kpc²), the systemic velocity ($v_{\text{sys}} = 300$ to 700 km/s), the velocity dispersion ($\sigma_v = 30$ to 200 km/s), and the turnover radius ($r_t = 10^{-4}$ to 6 kpc) and velocity ($v_t = 1$ to 1000 km/s).

For each combination of these parameters, we computed the total flux $S_{[\text{C II}]} = 2\pi I_0 h^2 \cos(i)$, the half-light radius $r_{[\text{C II}]} = 1.68 h$, the velocity at $2.2 h$, $v_{2.2} = (2 v_t/\pi) \arctan(2.2 h/r_t)$, the rotation period (or orbital time) $t_{\text{rot}} = 2\pi 2.2 h/v_{2.2}$ and the dynamical mass $M_{\text{dyn}} = 2.2 h v_{2.2}^2/G$.

The model best-fitting the observations was determined using a Levenberg-Marquardt minimization, assuming Gaussian statistics (see Bekiaris et al. 2016). We applied this fitting procedure to the observed cube, and determined the confidence intervals as in section 2.3: we created a set of simulated cubes by perturbing the best-fitting model with Gaussian noise, convolved them with the dirty beam, and applied the same fitting procedure to all the simulated cubes to obtain the distribution of best-fit values. The formal best-fit and residuals are shown on Figs. 1 and 5.

We found the systemic redshift of [C II] is $z = 3.7087 \pm 0.0004$, while the Balmer lines of *Jekyll* are at $z = 3.7174 \pm 0.0009$. The corresponding proper velocity difference is 549 ± 60 km/s, and is highly significant. Indeed, the uncertainty on the wavelength calibration of MOSFIRE is only 0.1 \AA or 1.3 km/s (Nanayakkara et al. 2016), and the observed frequency of ALMA is known by construction. In addition, both spectra were converted to the solar-system barycenter reference frame, and we used vacuum rest-wavelengths for both the Balmer and [C II] lines. The dominant source of uncertainty on the velocity offset is thus the statistical uncertainty quoted above.

The total line flux is $S_{[\text{C II}]} = 1.85 \pm 0.22$ Jy.km/s, which translates into a luminosity of $L_{[\text{C II}]} = (8.4 \pm 1.0) \times 10^8 L_{\odot}$. The inclination is relatively low, $i = 19$ to 55° , while the turnover radius is essentially unresolved, $r_t = 0_{-0}^{+0.16}$ kpc. The half-light radius of the [C II] emission is consistent with being the same as that of the dust continuum: $0.11 \pm 0.03''$ or 0.80 ± 0.24 kpc. The disk is rotating rapidly, with a period of only $t_{\text{rot}} = 8.4_{-2.8}^{+7.9}$ Myr and a high velocity of $v_{2.2} = 781_{-366}^{+218}$ km/s. Consequently the inferred dynamical mass is also high: $M_{\text{dyn}} = 1.3_{-0.8}^{+1.2} \times 10^{11} M_{\odot}$.

The [C II]-to-FIR ratio of $\log_{10}(L_{[\text{C II}]} / L_{\text{FIR}}) = -2.91_{-0.13}^{+0.19}$ is a factor 3.6 ± 1.3 lower than the normal value in the local Universe (Malhotra et al. 1997), which clearly places this galaxy in the “[C II] deficit” regime (see Fig. 13). This is discussed further in section 4.4.

3. Stellar emission

3.1. Photometry

Since *Jekyll* and *Hyde* are extremely close, we performed a careful deblending to see if we could detect the stellar emission of *Hyde*. We did this by modeling the profile of all galaxies within a radius of $15''$ with GALFIT (Peng et al. 2002) on the *Hubble* F160W image, using single Sérsic profiles of varying posi-

³ <https://github.com/bek0s/gbkit>

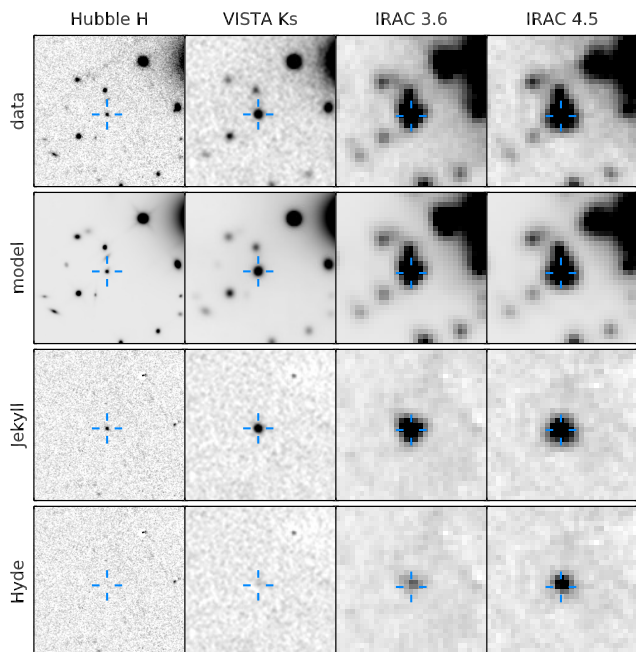


Fig. 6. Cutouts of the *Hubble* F160W, VISTA K_s , IRAC 3.6 and 4.5 μm (from left to right). The first row shows the original images, the second row shows our best model, the third row shows all sources subtracted except *Jekyll*, while the fourth row shows the same thing for *Hyde*. Each image is $18'' \times 18''$, and the color table is the same for all images in a given column. The position of *Jekyll* is indicated with a blue cross.

tion, total flux, half-light radius, position angle and Sérsic index. Since *Hyde* is not detected on the *Hubble* images, we assumed instead the disk profile obtained by modeling its dust emission (see section 2.3). We then used these profiles to build the models of all galaxies on the other bands using the appropriate point spread function (PSF), and fit the images as a linear combination of all these models plus a constant background (fluxes were allowed to be negative). Prior to the fit, the neighboring bright elliptical was modeled with four Sérsic profiles, adjusted with all other sources masked (including a lensed galaxy close to the core of the elliptical), and was subtracted from each image. A star spike was also removed from the *Hubble* images. Using this method, we extracted fluxes on all the Subaru, *Hubble*, ZFOURGE, VISTA and *Spitzer* IRAC broad-band images, covering $\lambda = 0.45$ to $8\mu\text{m}$. The result of this deblending depends on the assumption that the shape of all galaxies (including *Jekyll*) does not vary strongly between the *HST* H band and the other bands, in particular *Spitzer* IRAC. The clean residuals (see below and Fig. 6) suggest that this is not a major issue.

To estimate uncertainties, we performed a Monte Carlo simulation where we varied the noise in each image by extracting a random portion of empty sky from the residual image, and co-adding it on top of *Jekyll* & *Hyde*. This naturally accounts for correlated noise and large-scale background fluctuations. The PSFs were obtained by stacking stars in the neighborhood of our two galaxies, performing sub-pixel alignment using bicubic interpolation, except for *Spitzer* IRAC where we built a custom PSF by co-adding rotated version of the in-flight PSF matching the orientation of the telescope through the various AORs, weighted by their respective exposure time. Labbé et al. (2015) showed that the IRAC PSF is very stable in time, such that this procedure produces very accurate PSFs that can be used to go

deeper than the image’s confusion limit. Photometric zero points were matched to that of ZFOURGE (Straatman et al. 2016).

Obtaining an accurate de-blending of the *Jekyll* & *Hyde* pair required not only an excellent knowledge of the PSF, but also of the astrometry. To ensure our astrometry was well matched, we slightly shifted the WCS coordinate system of all the images until no residual remained for all the bright sources surrounding our two galaxies (to avoid biasing our results, the residuals at the location of *Jekyll* & *Hyde* were ignored in this process). These shifts were no larger than $0.05''$ for all bands but *Spitzer* IRAC, where they reached up to $0.1''$. Most importantly, we also randomly shifted the position of *Hyde*’s model in the Monte Carlo simulations used to estimate flux uncertainties, using a Gaussian distribution and the relative astrometry accuracy between ALMA and *Hubble* quantified in section 2.2 ($\sim 0.08''$). This step significantly increased the uncertainties in the *Spitzer* bands.

We could not validate the astrometry of the *Spitzer* IRAC 5.8 and $8\mu\text{m}$ images, since the S/N there is low and not enough sources are detected in the immediate neighborhood. For these bands we therefore only measured the total photometry of the *Jekyll* & *Hyde* system. The flux of *Jekyll* was then subtracted from these values, by extrapolation of the best-fitting stellar template (see next section). The remaining flux was attributed entirely to *Hyde*.

The resulting residual images are displayed in Fig. 6, and the fluxes are displayed in Fig. 9. We found that *Hyde* is clearly detected in the first two *Spitzer* IRAC channels ($[3.6] = 23.7$ and $[4.5] = 22.7$), barely detected in the K_s band ($K_s = 25.2$), and undetected in all the bluer bands, including those from *Hubble* (3σ upper limit of $H > 26.3$). This implies very red colors, $H - [4.5] = 5.1 \pm 0.8$, similar to that of “ H -dropout” galaxies (Wang et al. 2016), and strong attenuation by dust. We describe how we modeled this photometry in the next section and discuss the results of the modeling in section 3.3.

Even accounting for the uncertainty in the relative astrometry between ALMA and *HST*, the flux ratios between *Jekyll* and *Hyde* is well constrained. In the Monte Carlo simulations, the ratio $S_{Hyde}/(S_{Jekyll} + S_{Hyde})$ was $15^{+3}_{-2}\%$ and $28^{+6}_{-4}\%$ in the *Spitzer* 3.6 and 4.5 μm bands, respectively. Using a simpler χ^2 approach (i.e., ignoring the uncertainty on the relative astrometry), we obtained instead $15.4 \pm 0.8\%$ and $28.8 \pm 0.6\%$ (see Fig. 7, rightmost panel). The residuals obtained by fixing the flux ratio of *Jekyll* and *Hyde* to 0, 50 and 100% are shown in Fig. 7, and clearly show that either of these assumptions provides a poor fit compared to our best values of 15 and 28%. This demonstrates that *Hyde* is required to fit the IRAC emission, and that it cannot be brighter than *Jekyll*.

Lastly, we have also tried to fit the *HST* and *Spitzer* IRAC 4.5 μm images by freely varying the centroids (and for *HST* only, the profile shapes) of both *Jekyll* and *Hyde*. These fits therefore did not make use of *Hyde*’s centroid as observed in the ALMA image. In the *HST* image, we found that *Hyde* is offset from *Jekyll* by $\Delta\alpha = -0.11 \pm 0.05''$ and $\Delta\delta = +0.40 \pm 0.04''$, while in IRAC we found $\Delta\alpha = -0.047 \pm 0.02''$ and $\Delta\delta = +0.40 \pm 0.03''$. Both values are consistent with the ALMA position (offset of $0.02 \pm 0.08''$ and $0.09 \pm 0.06''$, respectively), which provides an independent evidence of *Hyde*’s existence as a separate source.

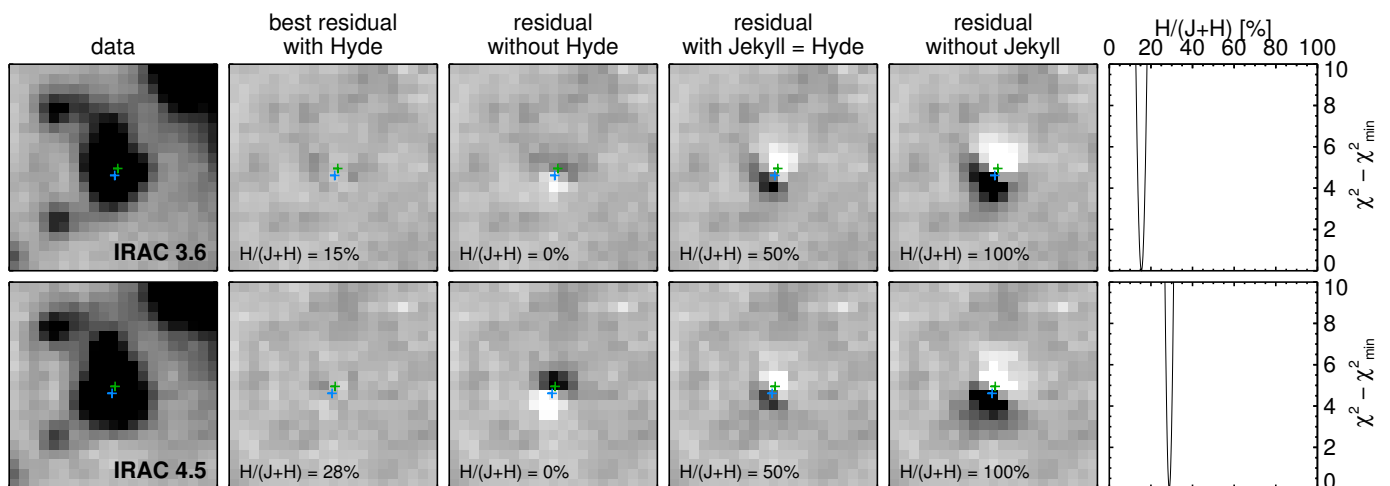


Fig. 7. Residuals of the *Spitzer* IRAC 3.6 (top) and 4.5 μm (bottom) images. From left to right: original image, best-fit residual, residual without *Hyde*, residual assuming the same flux for *Jekyll* and *Hyde*, residual without *Jekyll*, and χ^2 of the fit as a function of the flux ratio $S_{Hyde}/(S_{Jekyll} + S_{Hyde})$. Each cutout is $12'' \times 12''$, and the centroids of *Jekyll* and *Hyde* are shown with blue and green crosses, respectively.

3.2. Modeling

3.2.1. Description of the code and key assumptions

The photometry of both objects was modeled using FAST++⁴, a full rewrite of FAST (Kriek et al. 2009) that can handle much larger parameter grids and offers additional features. Among these new features is the ability to generate composite templates with any star-formation history (SFH) using a combination of Bruzual & Charlot (2003) single stellar populations. A second important feature is the possibility to constrain the fit using a Gaussian prior on the infrared luminosity L_{IR} , which can help pin down the correct amount of dust attenuation and improve the constraints on the other fit parameters. This code will be described in more detail in a separate paper (Schreiber et al. in prep.), and we provide a brief summary here for completeness.

The L_{IR} predicted by a given model on the grid is computed as the bolometric luminosity absorbed by dust, i.e., the difference in luminosity before and after applying dust attenuation to the template spectrum, assuming the galaxy’s flux is isotropic (see Charlot & Fall 2000; da Cunha et al. 2008; Noll et al. 2009). We thus used the values of L_{IR} determined in section 2.4 to further constrain the fit. Our adopted dust model is the same as that of FAST, and it assumes a uniform attenuation (A_V) for the whole galaxy. This implies that dust is screening all stars uniformly, regardless of their age, which is usually a crude assumption. Here we argue that there is little room for differential attenuation, given the small sizes of *Jekyll* and *Hyde* (see section 2.3) and the necessarily short timescales involved in their formation. A uniform screen model is therefore a reasonable choice. Compared to models which assume lower attenuation for older stars, the L_{IR} predicted by our model will tend to include a larger proportion of energy from old-to-intermediate age stars, and consequently, at fixed L_{IR} our model will allow lower levels of on-going star-formation (see also Sklias et al. 2017). This “energy balance” assumption has been shown to fail in strong starburst galaxies, possibly because of optically thick emission; these cases can be easily spotted as the model then provides a poor fit to the data (Sklias et al. 2017). This did not happen here.

As in FAST, a “template error function” is added quadratically to the flux uncertainties, taking into account the uncertainty in the stellar population model (in practice, this prevents the S/N in any single band from reaching values larger than 20, see also Brammer et al. 2008). This error function is not applied to the MOSFIRE spectrum of *Jekyll*. Instead, to reflect the fact that the relative flux between two spectral elements is more accurately known than their absolute flux, the code introduces an additional free normalization factor when fitting the spectrum. As a consequence, only the features of the spectrum contribute to the χ^2 (i.e., the strength of the absorption lines), and not its integrated flux.

Finally, we did not include emission lines in the fit. While $z = 3.7$ is the redshift where $H\alpha$ enters the IRAC 3.6 μm band, possibly contributing significantly to the broad-band flux (e.g., Stark et al. 2013), this is not a problem for our galaxies. Indeed, for *Jekyll* a contribution of more than 5% of the IRAC flux would require $\text{SFR} > 35 M_{\odot}/\text{yr}$, which is ruled out by the dust continuum and the absence of emission line in the K_s -band spectrum (Glazebrook et al. 2017). For *Hyde*, the modeling without emission line suggests $A_V = 3.5$ mag (see section 3.3), therefore a $> 5\%$ contribution of the 3.6 μm flux would require $\text{SFR} > 170 M_{\odot}/\text{yr}$, which is higher than that inferred from the infrared luminosity. The possibility of substantial contamination of the 3.6 μm band can thus be safely ignored here. The remaining potential contaminant is [O III], which could contribute to the K_s band flux. Because of the mask design, the MOSFIRE spectrum of *Jekyll* used by Glazebrook et al. did not cover this line. However, this system was later re-observed as filler in the MOSEL program (Tran et al. in prep.), with a 1.6 hours exposure in K and a different wavelength coverage including [O III]. No line was found in this new spectrum, and since the $0.7''$ slit is wide enough to include potential emission lines from *Hyde* as well, we confidently ignored strong emission lines in this analysis.

3.2.2. The grid

Fixing the redshifts to their spectroscopic values, we modeled the two galaxies using a “double- τ ” SFH, i.e., an exponential rise followed by an exponential decline (see Fig. 8). Compared to the

⁴ <https://github.com/cschreib/fastpp>

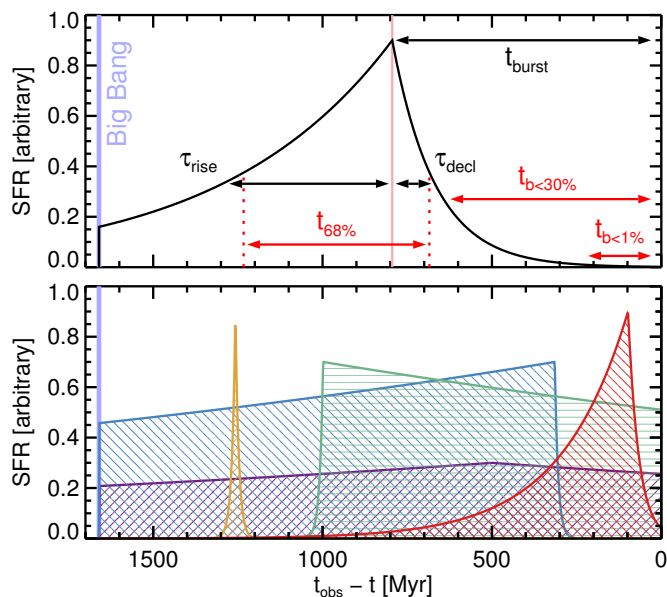


Fig. 8. Cartoon picture (top) and examples (bottom) of our model star-formation history, i.e., the SFR as a function of $t_{\text{obs}} - t$, where t_{obs} is the time of observation ($z \sim 3.7$). In the top row, we show the parameters of the model SFH in black, and the post-processed quantities in red. The examples shown in the bottom row are a roughly constant SFH since the Big Bang (purple), a roughly constant SFH starting 1 Gyr ago (green), a roughly constant SFH with an abrupt quenching 300 Myr ago (blue), a brief and old burst (yellow), and a slowly rising SFH with a recent decline (red). Many more combinations are possible but not shown for clarity.

top-hat SFH used in Glazebrook et al. (2017), this parametrization allows additional scenarios where the SFR is reduced gradually over time, rather than being abruptly truncated. The two phases can have different e -folding times, τ_{rise} and τ_{decl} , respectively. The corresponding analytic expression is

$$\text{SFR}(t) = C \times \begin{cases} e^{(t_{\text{burst}} - t)/\tau_{\text{rise}}} & \text{for } t > t_{\text{burst}}, \\ e^{(t - t_{\text{burst}})/\tau_{\text{decl}}} & \text{for } t \leq t_{\text{burst}}, \end{cases} \quad (1)$$

where t is the lookback time. The time of peak SFR, t_{burst} , was varied from 10 Myr to the age of the Universe (1.65 Gyr) in logarithmic steps of 0.05 dex. The two e -folding times, τ_{rise} and τ_{decl} , were varied from 10 Myr to 3 Gyr in steps of 0.1 dex. The constant C , which can be identified as the peak SFR, was finally used to adjust the normalization of the SFH for each combination of the above parameters, and eventually determined other derived properties such as the stellar mass. For each SFH, we computed the average SFR over the last 10 and 100 Myr ($\text{SFR}_{10\text{Myr}}$ and $\text{SFR}_{100\text{Myr}}$, respectively). In the following we refer to the ‘‘current’’ SFR as the average of the last 10 Myr, since variations of the SFR on shorter timescales are not constrained by the photometry; this average is thus better measured than the instantaneous SFR one would derive from Eq. 1.

The parameters t_{burst} , τ_{rise} and τ_{decl} were chosen to span a wide range of SFHs (as demonstrated in Fig. 8). However, their physical interpretation is not immediate, and the resulting parameter space contains some degeneracies. For example, the value of τ_{decl} is mostly irrelevant when t_{burst} is very small, and conversely the value of t_{burst} is also irrelevant when both e -folding times are large. We therefore post-processed the resulting SFHs to define a handful of well-behaved quantities. First,

defining $b = \text{SFR}(t)/\text{SFR}_{\text{max}}$ as the ratio between the instantaneous and maximum SFR, we computed the time spent with $b < 1\%$ and $b < 30\%$ starting from the epoch of observation and running backwards in time ($t_{b < 1\%}$ and $t_{b < 30\%}$, respectively). This can be identified as the duration of quiescence (t_{qu}), and will be equal to zero by definition if the galaxy is not quiescent at the time of observation. Second, we computed the shortest time interval over which 68 and 95% of the star-formation happened ($t_{68\%}$ and $t_{95\%}$, respectively), which can be identified as the formation timescale (t_{sf}). These quantities are illustrated in Fig. 8. Finally, to locate the main star-forming epoch, we computed the SFR-weighted lookback time $t_{\text{form}} = \int t \text{SFR}(t) dt / \int \text{SFR}(t) dt$ and the associated redshift z_{form} .

We then varied the attenuation from $A_V = 0$ to 6 magnitudes (assuming the Calzetti et al. 2000 absorption curve), and fixed the metallicity to the solar value (leaving it free had a negligible impact on the best fit values). A total of about 2 million models were generated and compared to the photometry of both galaxies. For *Jekyll* we also included the MOSFIRE spectrum, coarsely binned to avoid having to accurately reproduce the velocity dispersion of the absorption lines; in practice this amounts to introducing a prior on the Balmer equivalent widths. This resulted in 25 and 20 degrees of freedom for *Jekyll* and *Hyde*, respectively. Finally, confidence intervals were derived from the minimum and maximum values allowed in the volume of the grid with $\chi^2 - \chi^2_{\text{min}} < 2.71$ (i.e., these are 90% confidence intervals; Avni 1976). As a cross check, we also performed 1000 Monte Carlo simulations where the photometry of each galaxy was perturbed within the estimated uncertainties and fit as the observed photometry, and we then computed the 5th and 95th percentiles of the parameter distributions. The resulting constraints on the fit parameters were similar but slightly tighter than those obtained using the χ^2 criterion above; in order to be most conservative we used χ^2 -based confidence intervals throughout.

Using simulated bursty SFHs, we show in Appendix A that the resulting constraints on the quenching and formation timescales are accurate even if the true SFH deviates from the ideal model of Eq. 1. The only exception is when a second burst happened in the very early history of the galaxy. In these cases, two outcomes are possible: either the older burst is outshined by the latest burst and is thus mostly ignored (see also Papovich et al. 2001), leading to underestimated stellar masses and formation timescales, or the fit to the photometry is visibly poor, with discrepancies of more than 2σ in the NIR bands. On no occasion was a star-forming SFH misclassified as quiescent, instead small residual SFRs were found to potentially bias the quenching times to lower values.

Finally, we have tried to fit a more complex model than Eq. 1 to our galaxies by including a late exponentially rising burst active at the moment of observation, of variable intensity and e -folding time. The constraints for *Jekyll* were unchanged, and the only difference for *Hyde* was that additional solutions were allowed where the bulk of the galaxy formed very early ($z > 5$) in a short burst, while the observed FIR emission was produced by a more recent burst of lower SFR $\sim 80 M_{\odot}/\text{yr}$. These solutions appear unrealistic: the main burst of star-formation would have happened earlier than in *Jekyll* and yet the galaxy would still contain more dust than *Jekyll*. Given that this additional complexity did not provide further useful information but introduced unrealistic scenarios, we decided to keep the simpler SFH of Eq. 1.

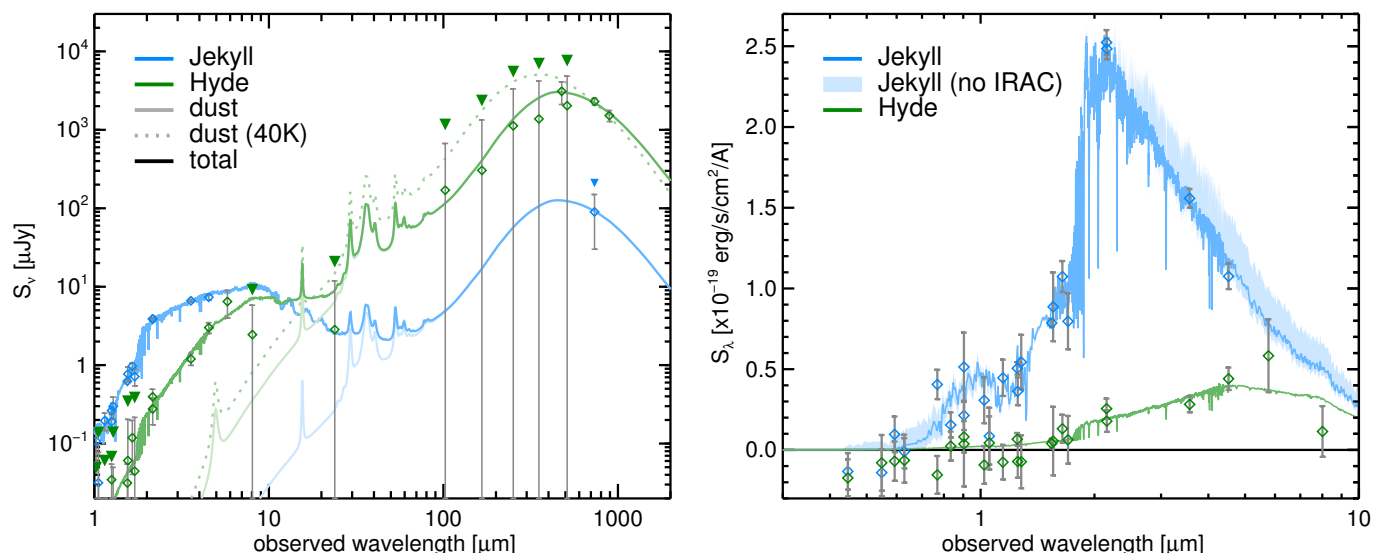


Fig. 9. Left: Photometry of *Jekyll* (blue) and *Hyde* (green) from the UV to the sub-millimeter. The observed photometry is shown with diamonds (downward pointing triangles indicate 2σ upper limits for measurements of significance less than 2σ). The best fitting dust model is shown with a pale line, and the total model (dust and stars) is shown with a darker line. For illustration, for *Hyde* we also show a dust model assuming $T_{\text{dust}} = 40\text{K}$, which overpredicts the MIPS, Herschel and SCUBA fluxes. The dust model for *Jekyll* is only illustrative, and was simply normalized to match the constraint from the $744\mu\text{m}$ flux. **Right:** Zoom-in on the stellar emission, shown in S_λ instead of S_ν . As described in the text, the 5.8 and $8\mu\text{m}$ photometry are shown here only for *Hyde*; the fluxes in these bands were obtained from aperture photometry of the whole system, with the predicted contribution of *Jekyll* subtracted. Here we also show in light blue the range of possible SEDs for *Jekyll* when all the IRAC photometry is ignored in the fit.

3.3. Results

The results of the UV-to-FIR SED modeling (section 3.2) are listed in Table 1 and illustrated in Fig. 10.

3.3.1. *Jekyll*

We recovered the result of Glazebrook et al. (2017), namely that *Jekyll* has quenched $>210\text{Myr}$ before we observed it, at $z \sim 5$, with a formation redshift between $z_{\text{form}} = 5.4$ and 7.6 . The sum of the quenched and star-forming epochs leads to a total age of $t_{b<30\%} + t_{68\%} = 610\text{Myr}$ to 1.1Gyr , which is slightly older than found by Glazebrook et al. Since some of the flux is now attributed to *Hyde*, the stellar mass of *Jekyll* has decreased by 30% (-0.14dex) compared to its initial estimation. The constraint from the observed L_{IR} rules out solutions with $A_V > 0.5$ for *Jekyll* and tends to push the formation timescale toward larger values, albeit still within the error bars quoted by Glazebrook et al. These changes are not sufficient to erase the tension with galaxy formation models, as the baryon conversion efficiency for a formation at $z = 5$ is still high (60%). Therefore the conclusions presented in Glazebrook et al. still apply.

We note that we reached this result even when we excluded the IRAC photometry from the fit; ignoring the IRAC fluxes would allow a larger stellar mass of up to $1.7 \times 10^{11} M_\odot$, but it would not impact the minimum mass. The rest of the data (i.e., mostly the K_s -band flux, $H - K_s$ color, L_{IR} limit, and MOSFIRE spectrum) indeed independently constrain the mass and SFH, and are sufficient to predict the IRAC 3.6 and $4.5\mu\text{m}$ fluxes of *Jekyll* with an accuracy of 24 and 28%, respectively (see Fig. 9, right). These results are thus insensitive to systematics in the IRAC de-blending. In addition, fitting only the U -to- K_s broadband photometry also leads to a lower limit on the mass of $1.0 \times 10^{11} M_\odot$; then, the SFH becomes poorly constrained and

the photometry allows dusty star-forming solutions with very extreme M/L , such that the maximum allowed mass increases to $2.9 \times 10^{12} M_\odot$. This shows that the red $H - K_s$ color alone places a stringent and secure lower limit on the M/L and the mass, since neither the H nor the K_s bands are significantly contaminated by *Hyde*.

A similar analysis of this galaxy pair was done in Simpson et al. (2017); they found a substantially lower mass of $0.8 \times 10^{11} M_\odot$ for *Jekyll*, which is below our minimum allowed mass. We attribute the source of this difference to the different UV-IR SED used for *Hyde*: using an average SMG SED and rescaling it to the observed ALMA flux for *Hyde*, Simpson et al. estimated a contamination of 30% to the K_s band (they predicted a flux of $\sim 1\mu\text{Jy}$). Instead, our explicit de-blending of the images showed that this value is only 6% ($0.33 \pm 0.08\mu\text{Jy}$); the ZFOURGE K_s -band has excellent spatial resolution ($0.47''$ FWHM), such that a 30% contribution to the flux would be readily apparent (e.g., Fig. 6). Their adopted SED also produces a higher contribution to the flux in the IRAC bands, albeit to a lesser extent. Da Cunha et al. (2015) showed that the rest-optical fluxes of SMGs spans two orders of magnitude at fixed sub-mm flux (see their Figure 13), which implies that a simple rescaling of the average SMG SED cannot predict accurate optical fluxes; an explicit de-blending and SED fit, as used here, is needed for accurate stellar masses.

3.3.2. *Hyde*

For *Hyde*, we found a large stellar mass either comparable to that of *Jekyll* or up to a factor three smaller, and a strong attenuation ($A_V \sim 3.5\text{mag}$) which is substantially redder than the average SMG ($A_V \sim 2$; da Cunha et al. 2015). The constraints on the star-formation history are looser than for *Jekyll*, however they are far from devoid of information. In particular, the

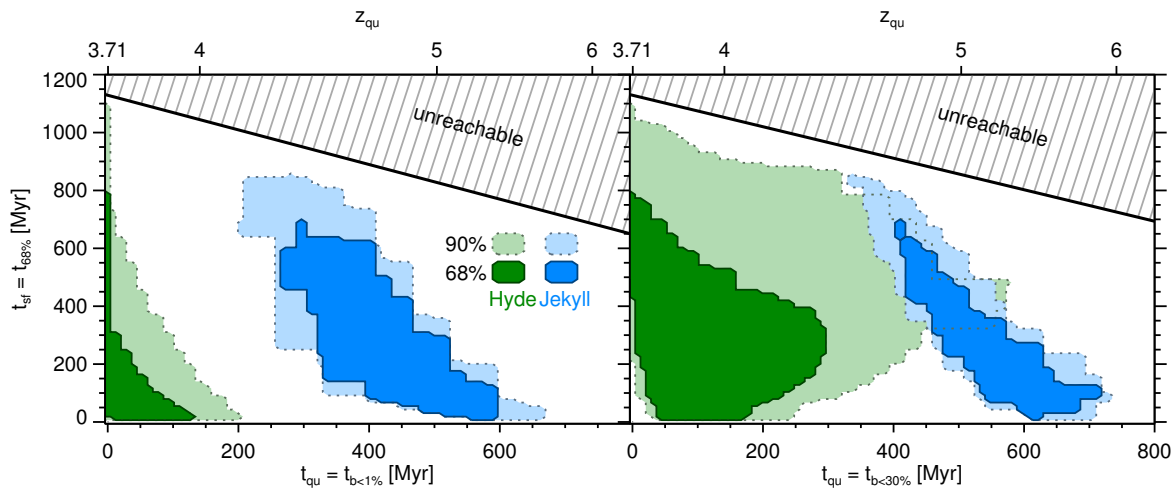


Fig. 10. Range of allowed values for the star-formation timescale (t_{sf}), defined as the time over which 68% of the star-formation happened, and the quiescence time (t_{qu}), defined either as the time spent with less than 1% (left) or 30% (right) of the peak SFR. The redshift at which the galaxy “quenched” is given on the top axis. The parameter spaces allowed for *Jekyll* and *Hyde* are shown in blue and green, respectively. The dark and light colored regions show the 68% and 95% confidence regions, respectively. The hashed region at the top indicates the part of the parameter space that would imply a formation before the Big Bang; such solutions were not explored.

photometry allows scenarios where star-formation was quenched ($b < 1\%$) up to 200 Myr prior to observation, and rules out current SFR higher than $120 M_{\odot}/\text{yr}$. In all the models allowed by the fit, the galaxy is located below the $z = 4$ main sequence by at least a factor 1.4 (Schreiber et al. 2017b). This includes scenarios where the galaxy is simply on the lower end of the main sequence (with a main sequence dispersion of 0.3 dex, there is a 30% chance of being located a factor 1.4 below the fiducial main sequence locus) as well as scenarios where the galaxy has recently stopped forming stars. Indeed, the SFR averaged over the last 10 or 100 Myr could also be zero, in which case the FIR emission in the model comes from obscured non-OB stars (e.g., Bendo et al. 2012, 2015; Eufrazio et al. 2017).

Other parameters like the formation timescale cover a broad range when marginalizing over the allowed parameter space. However, the allowed values span different ranges depending on whether *Hyde* has quenched or not (see Fig. 10). For quenched models with $t_{b<1\%} > 50$ Myr, $t_{68\%}$ can be at most 450 Myr (and less than 150 Myr at 68% confidence), and the current SFR $< 10 M_{\odot}/\text{yr}$. On the other hand, if the galaxy is still forming stars ($t_{b<30\%} = 0$) the formation timescale must be at least 250 Myr and the SFR averaged over the last 100 Myr must be less than $200 M_{\odot}/\text{yr}$. Therefore, either the galaxy has quenched after a brief but intense star-formation episode, or it has continuously formed stars at moderate rates over longer timescales. As we discuss in section 4, the compactness of the galaxy and the deficit of [C II] emission favor the former hypothesis.

Finally we note that the observed L_{IR} of *Hyde* provides crucial constraints on its modeled star-formation history. If L_{IR} had not been used in the fit, the whole parameter space would have been degenerate, and both the quiescence time and the formation timescale would be unconstrained.

4. Discussion

Using the diverse data and modeling presented in the previous sections, we now proceed to discuss the implications for the two galaxies studied in this paper.

While we were analyzing the data, Simpson et al. (2017) concurrently performed a similar analysis to that undertaken here, but using the shallower ALMA data in which the sub-millimeter emission was first detected, and without the information of the [C II] emission. Assuming the sub-millimeter emission originates from an obscured component within the same galaxy, they subtracted this obscured component from the total photometry using an average optical SED for SMGs and re-evaluated the stellar mass of the quiescent component. They concluded that the mass reported in Glazebrook et al. (2017) had been overestimated by a factor two or more, and that after correction the tension with models (e.g., Wellons et al. 2015; Davé et al. 2016) was erased. They further argued that sub-millimeter emission is not an unusual feature in so-called post-starburst galaxies, and implied that the galaxy may not be as old as it was initially claimed.

Based on the new ALMA data and an explicit de-blending of the UV-near-IR imaging, our findings are not consistent with those of Simpson et al. (2017). We obtained definite proof that the sub-millimeter emission is in fact produced by a separate galaxy (see section 4.2), which is extremely obscured. The colors of the dusty galaxy are redder than assumed by Simpson et al., resulting in a lower contamination of the photometry of the quiescent galaxy and a milder reduction of its stellar mass (see the discussion in section 3.3). The quiescent galaxy, in turn, is not detected in our deep dust continuum map, imposing a stringent upper limit on its obscured SFR. We discuss this further in the next section.

4.1. No significant dust-obscured star-formation in *Jekyll*

Simpson et al. (2017) argued that deep Balmer absorption lines, as observed in *Jekyll*, are not uniquely associated with truly post-starburst galaxies and can be observed in dusty starbursts as well. This can happen if the A stars, responsible for the Balmer absorption features, have escaped the dust clouds, where star-formation is still on-going and fully obscured. Such galaxies are labeled “e(a)” (Poggianti & Wu 2000). Simpson et al. quoted Mrk 331 as an example.

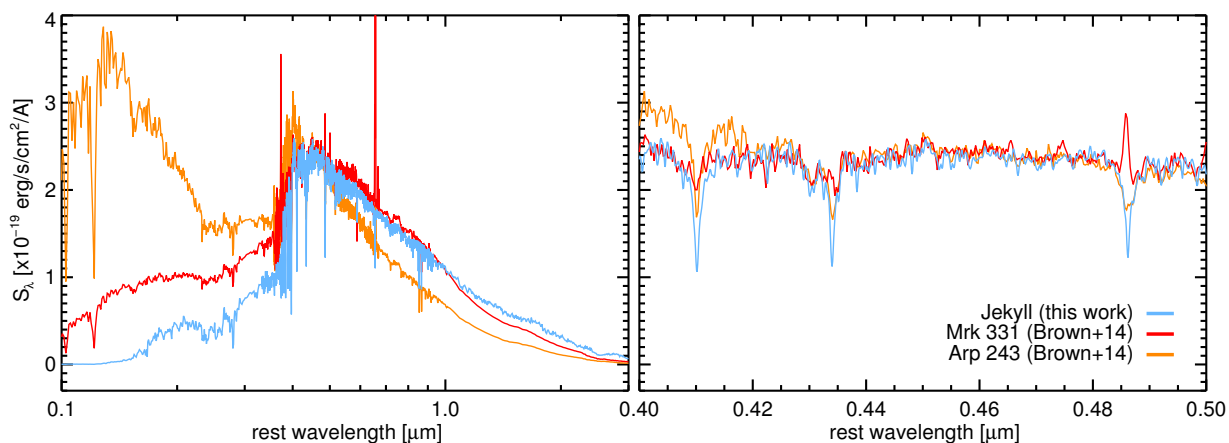


Fig. 11. Best stellar model of *Jekyll*, compared to the models of two local LIRGs with Balmer absorption lines, Mrk 331 and Arp 224, obtained by Brown et al. (2014). All these models use spectra to constrain the strength of the Balmer absorption lines (the spectra are not shown for clarity). The models of the two LIRGs were rescaled to match the continuum level of *Jekyll* at rest wavelengths between 0.45 and 0.48 μm .

We have shown in section 2.3 that there is no detectable sub-millimeter emission at the position of *Jekyll*, therefore the amount of obscured star-formation in this galaxy must be particularly small ($\text{SFR}_{\text{IR}} < 13 M_{\odot}/\text{yr}$ at 3σ , converting the limit on the observed L_{IR} to SFR directly, assuming no contribution of older stars to the dust heating). In the following, we nevertheless argue that *Jekyll* has very different spectral properties than those “e(a)” galaxies, and therefore the possibility of it belonging to this class of object could have been discarded from the start.

We display our best model for *Jekyll* and that of Mrk 331 as obtained by Brown et al. (2014) in Fig. 11. It is immediately apparent that Mrk 331 has a weaker Balmer break, implying a younger stellar population. But more importantly it has an $\text{H}\delta$ equivalent width of only 4.1 \AA , a factor two lower than that observed in *Jekyll*, and $\text{H}\beta$ in emission rather than absorption (see Poggianti & Wu 2000). It is thus clear that Mrk 331 is not a good analog of *Jekyll*.

Poggianti & Wu (2000) analyzed the Balmer equivalent widths of a complete sample of luminous infrared galaxies ($L_{\text{IR}} > 3 \times 10^{11} L_{\odot}$) drawn from the IRAS 2Jy catalog (see Wu et al. 1998). This catalog covers 35 000 square degrees with redshifts up to $z \sim 0.1$, which corresponds to a volume 300 times larger than that covered by ZFOURGE at $3.4 < z < 4.2$. Of the 52 galaxies with spectral coverage for both $\text{H}\beta$ and $\text{H}\delta$ (60% of their sample), none has $\text{EW}_{\text{H}\delta} > 7 \text{\AA}$ and $\text{EW}_{\text{H}\beta} > 7 \text{\AA}$, while *Jekyll* has $\text{EW}_{\text{H}\delta} = 9.8 \pm 2.6 \text{\AA}$ and $\text{EW}_{\text{H}\beta} = 19.2 \pm 4.2 \text{\AA}$ (NB: in their Table 1, Poggianti et al. listed the equivalent widths of $\text{H}\delta$ with positive values for absorption, but they used the opposite convention for $\text{H}\beta$). The closest match is Arp 243 (IRAS 08354+2555), with $\text{EW}_{\text{H}\delta} = 7.2 \text{\AA}$ and $\text{EW}_{\text{H}\beta} = 5.3 \text{\AA}$, which we also show on Fig. 11. While the absorption lines are stronger than in Mrk 331, the Balmer break is also much weaker.

Despite the larger volume of the IRAS catalog, no galaxy from this sample matches simultaneously the strong Balmer break, $\text{H}\delta$, and $\text{H}\beta$ absorption observed in *Jekyll*. It is therefore clear that *Jekyll* has little in common with “e(a)” galaxies, and its non-detection on our deep dust continuum map confirms this conclusion.

4.2. Hyde is a separate galaxy

Given the close proximity of *Jekyll* and *Hyde*, it is legitimate to wonder if these are, indeed, two separate galaxies or two components of a single galaxy. This distinction goes beyond mere semantics: if these are two different galaxies, their formation history can be studied separately as their stellar, dust, and gas component have never mixed. They can be considered as two closed boxes with no exchange of matter. On the other hand, if these were two regions of a single galaxy, it would be possible for matter to migrate from one region to the other, and only the summed star-formation history of both components would be meaningful. One could imagine, for example, that the entire galaxy has been forming stars continuously, and that old stars have migrated out of the dusty star-forming region a few hundred million years prior to observation.

The answer to this question therefore determines whether or not we have found a truly quiescent galaxy at $z \sim 4$. We stress however that there is one fact that holds regardless: the detection of the Balmer absorption lines in *Jekyll* imposes, without a doubt, that about $10^{11} M_{\odot}$ of stars were already formed at $z \sim 5$. The implied past SFR and its consequence on galaxy evolution models (see section 3.3 and Glazebrook et al. 2017) is not changed by this discussion.

Based on the data we present in this paper, a number of arguments can be put forward to show that indeed these are two separate galaxies. First, the large line-of-sight velocity difference of $\sim 550 \text{ km/s}$ demonstrates their existence as two kinematically separate components, rather than an homogeneous mixture of stars and dust. Second, the projected distance between *Jekyll* and *Hyde* corresponds to five times their respective half-light radii, which rules out the interpretation of this system as a smooth galaxy with an attenuation gradient. Indeed, while Chen et al. (2015) showed that physical offsets as large as $\Delta p = 3.3 \text{ kpc}$ are common when comparing the ALMA and *HST* emission of $z \sim 2$ SMGs, if caused by an attenuation gradient the amplitude of such offsets must naturally scale with a galaxy’s size. Chen et al. found an average stellar half-light radius of $r_{1/2} \sim 4 \text{ kpc}$ for their SMGs, implying an average $\Delta p/r_{1/2} \sim 0.8$. For a galaxy as small as *Jekyll*, this corresponds to a potential offset of the order of 0.4 kpc only, or $0.06''$, which is much smaller than the observed $0.43''$.

Table 1. Properties of *Jekyll* & *Hyde*.

	<i>Jekyll</i>	<i>Hyde</i>
z_{spec}	3.7174 ± 0.0009	3.7087 ± 0.0004
Dust properties		
$S_{744\mu\text{m}}$ (mJy)	0.09 ± 0.06	2.31 ± 0.14
r_{dust} (kpc)	–	0.67 ± 0.14
T_{dust} (K)	$20 - 35^a$	31^{+3}_{-4}
L_{IR} ($10^{12} L_{\odot}$) ^b	$0.036^{+0.031}_{-0.024}$	$1.1^{+0.4}_{-0.3}$
L_{FIR} ($10^{12} L_{\odot}$) ^c	$0.020^{+0.020}_{-0.014}$	$0.67^{+0.25}_{-0.22}$
SFR _{IR} (M_{\odot}/yr)	$3.6^{+3.1}_{-2.4}$	110^{+43}_{-33}
M_{dust} ($10^8 M_{\odot}$) ^d	$0.19^{+0.26}_{-0.13}$	$3.2^{+2.2}_{-1.0}$
Σ_{FIR} ($10^{11} L_{\odot}/\text{kpc}^2$)	–	$2.3^{+1.9}_{-1.0}$
[C II] properties		
$S_{[\text{C II}]}$ (Jy.km/s)	–	1.85 ± 0.22
$r_{[\text{C II}]}$ (kpc)	–	0.80 ± 0.24
$L_{[\text{C II}]}$ ($10^8 L_{\odot}$)	–	8.4 ± 1.0
$\log_{10}(L_{[\text{C II}]} / L_{\text{FIR}})$	–	$-2.91^{+0.19}_{-0.13}$
$v_{2.2}$ (km/s)	–	781^{+218}_{-366}
σ_v (km/s)	–	79^{+30}_{-37}
$T v_{2.2} / \sigma_v$	–	$9.8^{+6.3}_{-4.6}$
t_{rot} (Myr)	–	$8.4^{+7.9}_{-2.8}$
M_{dyn} ($10^{11} M_{\odot}$)	–	$1.3^{+1.2}_{-0.8}$
Inferred gas properties		
M_{gas} ($10^{10} M_{\odot}$)	< 3.5	$3.6^{+4.3}_{-1.9}$
f_{gas}	$< 25\%$	$12 - 70\%$
Σ_{gas} ($10^4 M_{\odot}/\text{pc}^2$)	–	$1.0^{+1.8}_{-0.6}$
t_{ff} (Myr)	–	$1.2^{+0.9}_{-0.6}$
Stellar properties (90% confidence intervals)		
M_* ($10^{11} M_{\odot}$)	$1.03 - 1.35$	$0.34 - 1.28$
r_* (kpc)	0.49 ± 0.12^e	–
Σ_* ($10^4 M_{\odot}/\text{pc}^2$)	$2.2 - 9.7$	$0.9 - 6.6^f$
A_V (mag)	$0.19 - 0.48$	$2.68 - 3.81$
SFR _{10Myr} (M_{\odot}/yr)	$0 - 0.48$	$0 - 119$
SFR _{10Myr} /SFR _{MS}	$0 - 10^{-3}$	$0 - 0.72$
SFR _{100Myr} (M_{\odot}/yr)	$0 - 0.65$	$0 - 828$
Σ_{SFR} ($M_{\odot}/\text{yr}/\text{kpc}^2$)	$0 - 0.18^g$	$0 - 61$
$t_{b<1\%}$ (Myr)	$210 - 661$	$0 - 204$
$t_{b<30\%}$ (Myr)	$337 - 724$	$0 - 570$
$t_{68\%}$ (Myr)	$22^g - 839$	$22^g - 1079$
$t_{95\%}$ (Myr)	$58^g - 1246$	$58^g - 1566$

^a This is the range of temperatures assumed to estimate L_{IR} and M_{dust} for *Jekyll* only. It is not a measurement. ^b 8 to $1000 \mu\text{m}$. ^c 42.5 to $122.5 \mu\text{m}$.

^d These dust masses correspond to a model with amorphous carbon grains, which provides values a factor 2.6 lower than the graphite-based models commonly used in the literature (e.g., Draine & Li 2007). ^e From Straatman et al. (2015), 68% confidence interval. ^f Assuming that stars follow the same profile as dust. ^g These values are limited by the minimum e -folding times allowed in the grid.

Third, the fact that their stellar masses are comparable rules out the possibility of *Jekyll* being a satellite clump in the disk of *Hyde*. This hypothesis could be suggested by the fact that low-mass UV-bright clumps are often found in the outskirts of SMGs

(e.g., Targett et al. 2013). Yet, beside its small size *Jekyll* has little in common with these clumps (see Guo et al. 2012): it is massive and old, and dominates the flux at all $\lambda \leq 4.5 \mu\text{m}$. In addition, the projected velocity predicted by our disk modeling at the position of *Jekyll* is $+289^{+54}_{-72}$ km/s, which is only half of the observed velocity offset of $+549 \pm 60$ km/s. Therefore, *Jekyll* cannot be part of *Hyde*'s disk.

The fourth and last evidence that these are two separate galaxies lies in the velocity structure of the [C II] line. Indeed, “double horn” velocity profiles like that shown on Fig. 1 can only be obtained with a flattened rotation curve, which implies that the [C II] emission is confined within its own dark matter halo (we tried building a model with a clump embedded in the halo of *Jekyll*, but this never produced such double-horn profile). Linear velocity gradients on scales larger than 0.6 kpc ($0.1''$) are ruled out by our disk modeling. A similar velocity profile could also be produced by two dispersion-dominated components of equal mass but different systemic velocity, e.g., an on-going merger of two dusty galaxies, but there is no evidence that the dust continuum emission has two spatial components. Ruling out this possibility would require a spectrum with a higher S/N than we have here. Finally, the interpretation of the [C II] emission generated by outflowing material from *Jekyll* is ruled out by the detection of dust and stellar continuum spatially-coincident with the line emission.

Given this suite of evidence, the hypothesis of this *Hubble* and ALMA emission coming from a single galaxy appears unlikely. We thus conclude that *Jekyll* and *Hyde* are indeed two separate galaxies, and therefore that *Jekyll* is a galaxy in which star-formation has uniformly stopped sometime around $z \sim 5$.

Incidentally, the spectroscopic redshift of *Hyde* constitutes one of the few robust redshift measurement of an “*H*-dropout” galaxy (see also Daddi et al. 2009b for GN-10 at $z = 4.04$ and Walter et al. (2012) for HDF-850.1 at $z = 5.18$). The *H*-dropout population was first identified in the *Spitzer* IRAC images as sources having no counter-part in the deep *H* or *K*-band images, implying high redshifts, large stellar masses and extreme obscuration (e.g., $H - [4.5] > 2.5$, Huang et al. 2011; Caputi et al. 2015; Wang et al. 2016). This obscuration makes it impossible to determine redshifts using nebular lines, and their SEDs are also lacking identifiable features such as the Lyman or Balmer break so their photometric redshifts are poorly constrained. Wang et al. (2016) showed that, if all at $z \sim 4$, these galaxies could contribute significantly to the mass function and cosmic SFR density, but were previously missing from most high redshift census. The confirmation of *Hyde* at $z \sim 4$ supports this result and highlights the importance of better understanding this population.

4.3. Compactness as a tracer of quenching

Hyde has very compact dust emission, $r_{1/2} < 1$ kpc. From the absence of NIR emission in the outskirts of the galaxy (as could have been detected by *Hubble*), we assumed that dust is well mixed with the stars, and therefore that the stellar size must be comparable to the dust size. As shown in Fig. 12, for a stellar mass above $4 \times 10^{10} M_{\odot}$ at $3.4 < z < 4.2$, only one or two of the 14 other star-forming galaxies (SFGs) in ZFOURGE with *HST* coverage have $r_{1/2} < 1$ kpc; instead, this size is typical for quiescent galaxies (Straatman et al. 2015; and see also Allen et al. 2017). The size of *Hyde* is in fact remarkably similar to that of *Jekyll* ($r_{1/2} = 0.49 \pm 0.12$ kpc; Straatman et al. 2015).

Similarly compact SFGs have been found at higher redshifts ($z \sim 4.5$), albeit with SFRs larger by an order of magnitude, and were interpreted as being triggered by major mergers (Oteo et al.

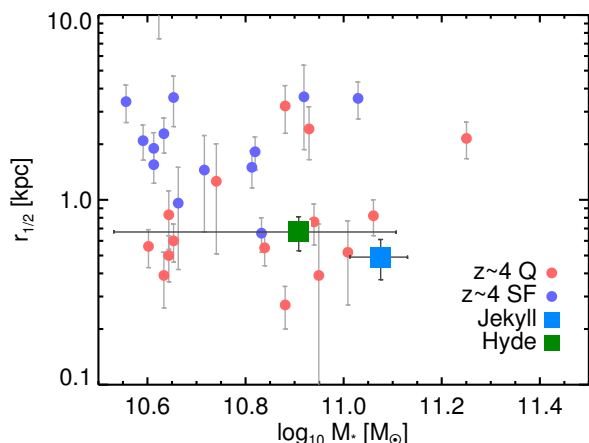


Fig. 12. Relation between the half-light radius ($r_{1/2}$) and the stellar mass for ZFOURGE galaxies with *HST* coverage (80% of the whole sample). *Jekyll* and *Hyde* are shown as blue and green squares, respectively, and are compared to other $z = 4$ galaxies in the same field (Straatman et al. 2015). Star-forming galaxies are shown in blue, quiescent galaxies in red. The half-light radii are derived from the *Hubble* F160W imaging (hence, rest-frame *U* band) for all galaxies except *Hyde*, for which the radius is that of the dust continuum.

2016). Post-starburst galaxies at $1 < z < 2$ have sizes similar to quiescent galaxies (Almaini et al. 2017), implying that the increase in compactness must happen within a short period of time surrounding the quenching event. In fact, the relation between stellar surface density and specific SFR of all galaxies in this redshift range suggests that SFGs become compact before they quench (Barro et al. 2013). However, the converse appears to be true at $z = 0$: among galaxies with strong $H\delta$ absorption, only those post-starburst galaxies with no detectable star-formation have the size and morphology of quiescent galaxies (Wilkinson et al. 2017). This suggests that, in the present day, the increased in compactness happens after star-formation has started to decline, and therefore that different quenching mechanisms have acted throughout the history of the Universe (e.g., Schreiber et al. 2016).

In the high-redshift context, a compelling evolutionary link can be drawn in which *Hyde* has formed rapidly through major mergers, building up its dense stellar core, and is now on its way to become a quiescent galaxy not unlike its companion *Jekyll*. One could even speculate that this burst of star-formation was triggered (or, indeed, terminated) by a recent interaction with *Jekyll* (see section 4.6). This would be consistent with the scenario suggested by the SED modeling in which *Hyde* has just quenched or is in the process of quenching.

Assuming that all galaxies must grow a compact core before they quench, Barro et al. (2013) found that compact $z \sim 2$ SFGs had to become quiescent rapidly, within 300 to 1000 Myr. Straatman et al. (2015) also showed that compact SFGs remained rare both at $z \sim 4$ and $z \sim 3$ ($\sim 7\%$ of the SFGs), supporting the idea that compact SFGs cannot remain star-forming for very long. We therefore concluded that *Hyde* must be observed in this brief phase leading to quenching. Since the growth of a compact core supposedly precedes quenching, this argument does not allow us to determine if *Hyde* has already quenched or not, only that it must be observed within 300 to 1000 Myr of its quenching. Given that *Hyde* is located at least a factor two below the main

sequence, it is however probable that the quenching process has already started, and perhaps even ended.

4.4. The cause of the low $L_{[\text{C II}]} / L_{\text{FIR}}$ ratio

We now turn to interpreting the low $L_{[\text{C II}]} / L_{\text{FIR}}$ ratio of *Hyde* in light of the above discussion.

4.4.1. Comparison to known galaxies and trends

We show in Fig. 13 (left) a compilation of $L_{[\text{C II}]} / L_{\text{FIR}}$ measurements for both low- and high-redshift galaxies. At the luminosity of *Hyde* ($L_{\text{FIR}} \sim 10^{12} L_{\odot}$), $[\text{C II}]$ deficits are typical in the local Universe (e.g., Díaz-Santos et al. 2013) but become rare at high redshifts (e.g., Brisbin et al. 2015; Gullberg et al. 2015; Capak et al. 2015; Schaerer et al. 2015; Smit et al. 2017), except perhaps in quasars (e.g., Venemans et al. 2016). In fact, searching the literature we found only three high-redshift galaxies with similar $L_{[\text{C II}]} / L_{\text{FIR}}$ and $L_{\text{FIR}} \lesssim 10^{12} L_{\odot}$: the lensed galaxy observed by Schaerer et al. (2015) at $z \sim 2$, and the galaxies found by Trakhtenbrot et al. (2017) in the vicinity of $z \sim 4.5$ quasars.

The galaxy studied by Schaerer et al. is located a factor ~ 20 above the main sequence (Sklias et al. 2014, see also Fig. 13, right) and is thus an extreme starburst. Such galaxies are known to have systematically lower $L_{[\text{C II}]} / L_{\text{FIR}}$ ratios in the local Universe (Díaz-Santos et al. 2013): indeed, essentially all the galaxies with $L_{[\text{C II}]} / L_{\text{FIR}} < 10^{-3}$ in the sample of Díaz-Santos et al. have $\text{SFR} / \text{SFR}_{\text{MS}} > 3$, thus in the local Universe $[\text{C II}]$ deficits mainly correspond to unusually high star-formation activity. As shown on Fig. 13, a similar trend can be observed at higher redshifts: apart from the galaxies from Trakhtenbrot et al. (which we discuss below), all galaxies with $L_{[\text{C II}]} / L_{\text{FIR}} < 5 \times 10^{-3}$ are at least a factor of two above the main sequence. In contrast, the more normal $z \sim 5$ LBGs (Capak et al. 2015; Smit et al. 2017) and $z \sim 2$ galaxies (Brisbin et al. 2015) have no deficit. *Hyde* is located below the main sequence by a factor of two or more (see Fig. 13, right), and is thus not a starburst galaxy. This suggests the cause for the deficit in *Hyde* must be different from that of the Schaerer et al. galaxy and of the other luminous starbursts.

The $z = 4.5$ galaxies of Trakhtenbrot et al. are more moderate systems, as they lie within the scatter of the main sequence or even below it. These should thus be more directly comparable to *Hyde*, although we caution that their masses, SFR and L_{FIR} are only poorly constrained (L_{FIR} are estimated from a single flux measurement, their dust temperatures being unknown, and stellar masses are based on dynamical masses). The fact that these galaxies are satellites of bright quasars, which are believed to soon turn into quiescent galaxies, is reminiscent of the proximity of *Hyde* and *Jekyll*. It is unknown whether *Jekyll* did go through a quasar phase while quenching, but if super-massive black holes do reside in the cores of all galaxies, then given *Jekyll*'s high stellar mass and compact size, a past quasar phase seems difficult to avoid (see also section 4.5). One could then speculate that the depleted $[\text{C II}]$ emission could reflect a modification of the gas properties caused either by gravitational interaction with a massive neighbor, or by the quasar's intense radiation.

More generally, it is observed in the local Universe that the $L_{[\text{C II}]} / L_{\text{FIR}}$ ratio is tightly correlated with the surface density of IR luminosity (Σ_{FIR} ; Lutz et al. 2016; Díaz-Santos et al. 2017) or equivalently with the SFR density. The origin of this relation is not clear, but it seems to hold over multiple orders of magnitudes of Σ_{SFR} , at both low and high redshifts (Smith et al. 2017). Despite its moderate L_{IR} , *Hyde* has an unusually small size and its

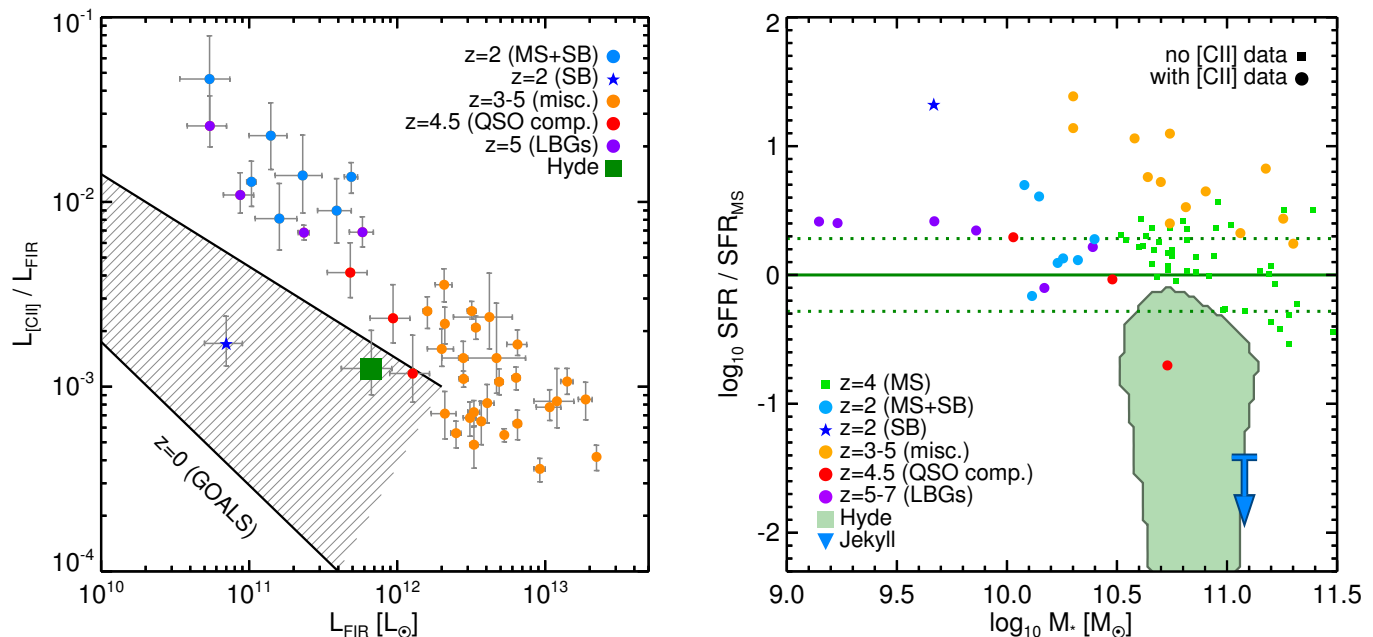


Fig. 13. Left: Relation between the $L_{[\text{C II}]} / L_{\text{FIR}}$ ratio and L_{FIR} . The values observed for *Hyde* are shown with a green square. The range of values found in $z = 0$ luminous infrared galaxies are indicated with the hashed region (Díaz-Santos et al. 2013). High-redshift galaxies from the literature are shown with colored circles: light blue for the $z = 2$ galaxies of Brisbin et al. (2015), dark blue for the lensed $z = 2$ galaxy studied in Schaerer et al. (2015), red for the $z = 4.5$ SMGs found near quasars in Trakhtenbrot et al. (2017), purple for the $z = 5$ LBGs of Capak et al. (2015), and finally orange a collection of galaxies at $z = 3$ to 5 (Cox et al. 2011; De Breuck et al. 2011; Valtchanov et al. 2011; Swinbank et al. 2012; Walter et al. 2012; Wagg et al. 2012; Riechers et al. 2013, 2014; Gullberg et al. 2015; Oteo et al. 2016). Galaxies from Brisbin et al. and Gullberg et al. with unknown magnification factors were assumed to have $\mu = 10$ (the average of the published magnifications from both samples). When needed, we assumed $L_{\text{FIR}} = L_{\text{IR}} / 1.5$. **Right:** Relation between the offset from the main sequence ($\text{SFR} / \text{SFR}_{\text{MS}}$) and the stellar mass for the galaxies on the left with measured masses. If no stellar mass estimate was available, we inferred it from the dynamical mass assuming a gas fraction of 50%. The value of SFR_{MS} was taken from Schreiber et al. (2015) at $z < 3.5$ and Schreiber et al. (2017b) at $3.5 \leq z \leq 4.5$; values at higher redshifts were estimated assuming a redshift dependence of $(1+z)^{1.5}$. On this plot, we also show with purple circles the two $z = 6.6$ LBGs of Smit et al. (2017), which are detected in [C II] but not in the FIR continuum, and thus for which the SFR is based only on the UV luminosity. We also show the position of $z = 4$ main sequence galaxies from Schreiber et al. (2017b) as small green squares; these galaxies have no [C II] measurement. The 90% confidence region for *Hyde* is shown in light green, and the most conservative upper limit of *Jekyll* ($\text{SFR} < 13 M_{\odot} / \text{yr}$ at 3σ , as obtained from SFR_{IR}) is shown with a blue arrow for reference.

IR density is relatively high: $\Sigma_{\text{FIR}} = (2.3^{+1.9}_{-1.0}) \times 10^{11} L_{\odot} / \text{kpc}^2$. According to the $L_{[\text{C II}]} / L_{\text{FIR}} - \Sigma_{\text{FIR}}$ relation of Lutz et al. (2016), this value should correspond to $\log_{10}(L_{[\text{C II}]} / L_{\text{FIR}}) = -3.2$ to -2.9 , which is in very good agreement with our observed ratio.

In most galaxies, L_{FIR} is a direct tracer of SFR and both quantities have thus been used interchangeably to investigate the cause of the [C II] deficit. Yet there is a physical difference between L_{FIR} and SFR: L_{FIR} may only represent the obscured SFR, and it may also include contributions from energy sources other than recent star-formation (e.g., older stars, or AGNs). Observationally, it is actually unknown which of L_{FIR} or SFR is best related to the [C II] luminosity.

4.4.2. A softer radiation field?

Interpreting the [C II] line flux from the point of view of physical conditions in the interstellar medium (ISM) is not straightforward since [C II] can originate from multiple phases of the ISM (e.g., Stacey et al. 1991; Madden et al. 1993), and there are therefore a number of ways to explain a deficit (Malhotra et al. 2001). In nearby galaxies, the majority of the [C II] emission originates from photo-dissociation regions (PDRs; Stacey et al. 2010). In this environment, carbon is easily ionized, and

the excitation of the fine-structure [C II] emission is provided by collisions with gas particles, themselves heated by interactions with free electrons (Tielens & Hollenbach 1985; Stacey et al. 2010). These electrons are extracted from small dust grains and polycyclic aromatic hydrocarbon (PAH) molecules through the photoelectric effect of far UV photons emitted by nearby young stars (Weingartner & Draine 2001). Therefore the [C II] emission is ultimately tied to the ambient far-UV radiation.

One possible explanation for a low $L_{[\text{C II}]} / L_{\text{FIR}}$ ratio would thus be a softer stellar radiation field (Nakagawa et al. 1995; Luhman et al. 1998; Kapala et al. 2017; Lapham et al. 2017): [C II] is depressed by a lack of PAH-ionizing photons ($E > 6$ eV, mostly emitted by O and B stars), while residual IR emission is still produced by heating from less energetic photons (mostly produced by intermediate-age stars). This would imply a recent diminution of star-formation, which we quantify in the next paragraph. As noted in Malhotra et al. (2001), this scenario cannot be the right explanation for all the [C II]-deficient galaxies since it would imply that all starburst galaxies are observed after a substantial reduction of their star-formation activity. But in our case it is consistent with *Hyde* being located below the main sequence, as well as with the model of Díaz-Santos et al. (2017): at $T_{\text{dust}} = 31$ K and $\log_{10}(L_{[\text{C II}]} / L_{\text{FIR}}) = -2.91$, they predict that only half of the [C II] emission is coming from dense PDRs; the

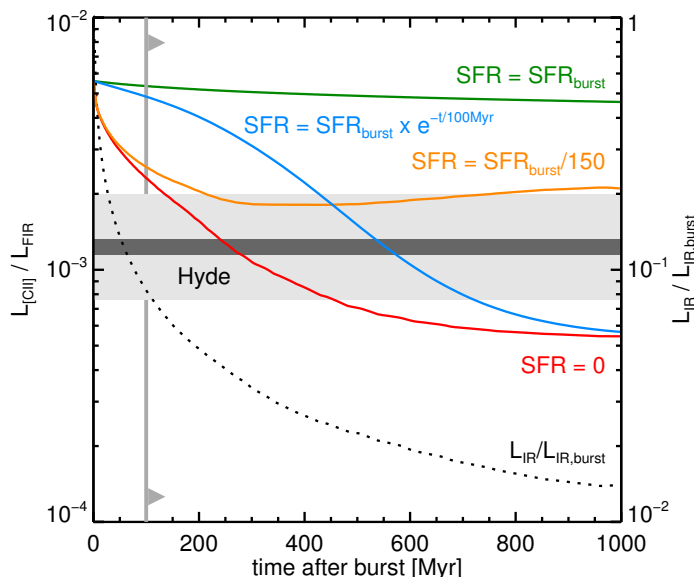


Fig. 14. Ratio of the luminosity of the [C II] line ($L_{[\text{C II}]}$) to the far-IR luminosity (L_{FIR} , 42.5 to 122.5 μm) produced by a composite stellar population, as predicted by the toy model described in the text. These values correspond to a stellar population created in a single burst from $t = -100$ to $t = 0$ Myr, and with varying amounts of residual star-formation after the burst. The red line shows the case where there is no residual star-formation, while the orange curve corresponds to a residual SFR 150 times lower than the SFR during the burst. The blue line corresponds to an exponentially declining SFR after the burst, with timescale 100 Myr. The green line shows the case of constant star-formation for reference (i.e., no end to the burst). The [C II] deficit of *Hyde* and its error bar are indicated with a dark gray band and shaded region in the background. Lastly, the relative decrease of L_{IR} with time in the case of no residual star-formation is shown with a dotted line.

rest of the emission is produced in regions of hot, diffuse ionized gas (see also Croxall et al. 2017). There, ionization can be caused by sources other than young stars, such as post-AGB stars, shocks, or an active galactic nucleus (see Annibali et al. 2010 and references therein).

4.4.3. A toy model using composite stellar populations

We thus built a toy model to estimate the timescale over which a reduced SFR could cause an observable [C II] deficit (see also Kapala et al. 2017 where a similar approach was used). Since the [C II] emission in PDRs is ultimately modulated by the ionization of dust grains and PAHs, it will respond to the incident flux of photons with $6 \lesssim E < 13.6$ eV ($912 < \lambda \lesssim 2000$ Å; Stacey et al. 2010), so $L_{[\text{C II}]}^{\text{PDR}} \propto L_{E>6\text{eV}}$. Since *Hyde* is strongly attenuated (see section 3.3), one can assume that $L_{\text{IR}} = L_{\text{bol}}$, and since $L_{\text{FIR}} \approx 0.61 L_{\text{IR}}$ for *Hyde*, the ratio $L_{E>6\text{eV}}/L_{\text{bol}}$ is a proxy for $L_{[\text{C II}]}^{\text{PDR}}/L_{\text{FIR}}$.

Considering a stellar population formed in a 100 Myr burst followed by varying amounts of residual star-formation, including a continuation of the burst, we computed the time dependence of $L_{E>6\text{eV}}$ and L_{bol} using the Bruzual & Charlot (2003) stellar population synthesis model (the composite stellar population was built using FAST++). Assuming stars always remain in their birth cloud, we first estimated an empirical conversion between $L_{E>6\text{eV}}$ and $L_{[\text{C II}]}^{\text{PDR}}$. For a system forming stars at a constant rate, after 100 Myr the ratio $L_{E>6\text{eV}}/L_{\text{bol}}$ is equal to 0.68 (this

value decreases only mildly with time afterwards, reaching 0.59 after 600 Myr). This should correspond to the average $L_{[\text{C II}]}^{\text{PDR}}/L_{\text{FIR}}$ ratio for star-forming galaxies. Diaz-Santos et al. (2017) show that, for a galaxy of $T_{\text{dust}} \sim 30$ K, the $L_{[\text{C II}]}^{\text{PDR}}/L_{\text{FIR}}$ ratio is on average 0.9%, from which we derived $L_{[\text{C II}]}^{\text{PDR}} = 7.5 \times 10^{-3} L_{E>6\text{eV}}$. For the diffuse ionized gas component, this same model predicts $L_{[\text{C II}]}^{\text{ion}}/L_{\text{FIR}} = 0.05\%$, which we assumed is independent of the stellar radiation field. The observed $L_{[\text{C II}]}/L_{\text{FIR}}$ is then the sum of these two components:

$$\frac{L_{[\text{C II}]}}{L_{\text{FIR}}} = \frac{L_{[\text{C II}]}^{\text{PDR}}}{L_{\text{FIR}}} + \frac{L_{[\text{C II}]}^{\text{ion}}}{L_{\text{FIR}}} = 1.3 \times 10^{-2} \frac{L_{E>6\text{eV}}}{L_{\text{bol}}} + 5 \times 10^{-4}. \quad (2)$$

Based on the sample of Diaz-Santos et al. (2017), we expect the scatter in both terms of this formula to be of the order of 0.2 dex. We finally stress that the above equation only applies to galaxies with $T_{\text{dust}} \sim 30$ K, the numerical constants being dependent on the temperature.

4.4.4. Comparison with the deficit of *Hyde*

The evolution of $L_{[\text{C II}]}/L_{\text{FIR}}$ predicted by this simple model is shown in Fig. 14 for various star-formation histories following the initial burst. In the case with no residual star-formation, the model predicts the $L_{[\text{C II}]}/L_{\text{FIR}}$ ratio decreases by a factor 3 about 100 Myr after the burst. If instead star-formation continues after the burst at a rate even 150 times lower than during the burst, the deficit barely reaches that observed in *Hyde*, suggesting that little on-going star-formation is allowed. If the decline in SFR is more gradual, with $\text{SFR} \sim e^{-t/\tau}$ and $\tau = 100$ Myr, a drop of a factor 3 is reached 400 Myr after the burst. Therefore, deficits such as the one we observe can be explained if the galaxy is observed more than 100 Myr after the end of an intense star-formation episode, with an additional lag if star-formation was reduced gradually rather than immediately. On the other hand, these timescales could be shorter if stars were allowed to leave their birth cloud early (e.g., after 100 Myr; Charlot & Fall 2000), or if the deficit of [C II] is only partly caused by a reduced star-formation (in which case the “baseline” value for a constant SFR would be lower to begin with, and it would take less time to reach the observed value).

This is consistent with the constraints on the quiescent time for *Hyde* obtained from the SED modeling, and would favor the scenario where the galaxy has just stopped forming stars. In the case of no residual star-formation, the L_{IR} observed 100 Myr after the burst is 12 times lower than the peak value during the burst (see dotted line in Fig. 14): for *Hyde*, this would imply a peak SFR of $\sim 1000 M_{\odot}/\text{yr}$ leading to a formation timescale of only 50 Myr, which is also consistent with the SED modeling and observation of strong starbursts at higher redshifts (e.g., Daddi et al. 2009a; Riechers et al. 2013; Oteo et al. 2016). This also implies that the galaxy cannot be observed too late after a burst, in which case the residual dust continuum emission would be weak, and the inferred SFR during the burst would reach values that have never been observed ($\text{SFR} > 10^4 M_{\odot}/\text{yr}$).

Finally, if we were to directly apply Eq. 2 to the range of SFHs allowed by the SED modeling, including the expected scatter, we would predict an observed $\log_{10}(L_{[\text{C II}]}^{\text{PDR}}/L_{\text{FIR}})$ ranging from -2.75 to -1.98 for the quenched SFHs ($t_{b<1\%} > 50$ Myr), which encompasses the measured value within the error bar, and -2.43 to -1.85 for the star-forming SFHs ($t_{b<30\%} = 0$), which is too high by at least 2.5σ . Our toy model is fairly rudimentary so this comparison can only be indicative, but it does suggest that the star-forming solutions are disfavored.

These conclusions could be validated by observing other far-IR lines which uniquely trace diffuse ionized gas, such as $[\text{N II}]_{205}$, and determine what fraction of the $[\text{C II}]$ is actually produced in PDRs without relying on the $z = 0$ results of Diaz-Santos et al. (2017).

4.5. Star-formation efficiency

To understand the star-formation processes in *Hyde* and determine which process may be at play, it is useful to estimate its star-formation efficiency and gas fraction.

4.5.1. Estimating the efficiency

From the results of the SED modeling, we constrained the current SFR of *Hyde* to be less than $119 M_{\odot}/\text{yr}$ at 90% confidence, and possibly zero. Given the size measured in the band 8 image, this translates into an 90% confidence upper limit on the SFR surface density, $\Sigma_{\text{SFR}} = (\text{SFR}/2)/(\pi r_{1/2,\text{dust}}^2) < 61 M_{\odot}/\text{yr}/\text{kpc}^2$. If we consider the models where *Hyde* has quenched, this could be further reduced to $\Sigma_{\text{SFR}} < 5.1 M_{\odot}/\text{yr}/\text{kpc}^2$.

To compute the gas surface density, we can assume the $[\text{C II}]$ line traces the geometry of the gas in the galaxy, but estimating the gas mass is harder. We can follow two independent approaches: first, using the dust mass and assuming a gas-to-dust ratio, and second, using the $[\text{C II}]$ line luminosity.

The far-IR SED of *Hyde* does not precisely constrain the dust mass, but we can nevertheless use it to obtain an order-of-magnitude estimate of the gas mass. In Schreiber et al. (2016), we have calibrated the gas-to-dust ratio (δ_{GDR}) of our adopted dust library against CO and H I measurements of local galaxies; these gas-to-dust ratios are higher than would be obtained with other dust models, such as the Draine & Li (2007) model, since the assumed dust chemical composition is different. We found $\delta_{\text{GDR}} = (155 \pm 23) \times (Z_{\odot}/Z)$, where Z is the gas-phase metallicity, with a residual scatter of 0.2 dex. The metallicity of *Hyde* is unknown, however given its large dust content it is probably close to solar. In all the following calculations we assumed solar metallicity, with an uncertainty of a factor two. Folding in all these uncertainties, the dust mass translates to a gas mass of $M_{\text{gas}}^{\text{dust}} = 5.9^{+8.6}_{-3.6} \times 10^{10} M_{\odot}$. This mass includes helium and hydrogen, the latter in both the molecular and atomic phases.

Alternatively, we can use the empirical $[\text{C II}]-\text{CO}(1-0)$ correlation derived for $z = 2$ galaxies in Gullberg et al. (2015) and $\alpha_{\text{CO}} = 2 M_{\odot}/(\text{K km/s}/\text{pc}^2)$ (from Swinbank et al. 2011, which we assume scales as $1/Z$, see Leroy et al. 2011). Taking into account the scatter in the $[\text{C II}]-\text{CO}(1-0)$ relation and the metallicity, we obtained $M_{\text{gas}}^{[\text{C II}]} = 2.9^{+3.7}_{-1.6} \times 10^{10} M_{\odot}$. This mass should only include the molecular hydrogen, but it is nevertheless consistent with the dust-based value.

Averaging these two independent estimates with inverse variance weighting, we finally obtained a gas mass of $M_{\text{gas}} = 3.6^{+4.3}_{-1.9} \times 10^{10} M_{\odot}$, which is well within the range allowed by the dynamical and stellar masses (see section 2.5). Given the upper limit on the SFR, this translates into a lower limit on the depletion time $t_{\text{dep}} = M_{\text{gas}}/\text{SFR} > 144 \text{ Myr}$, or 1.8 Gyr if *Hyde* has quenched.

Using the $[\text{C II}]$ spatial extent, we derived $\Sigma_{\text{gas}} = (M_{\text{gas}}/2)/(\pi r_{1/2,[\text{C II}]}^2) = (1.0^{+1.8}_{-0.6}) \times 10^4 M_{\odot}/\text{pc}^2$. This is among the largest values ever measured: for example the $z = 6.3$ “maximum starburst” HFLS-3 has $\Sigma_{\text{gas}} = 1.4 \times 10^4 M_{\odot}/\text{pc}^2$ (Riechers et al. 2013). Yet, this same galaxy has an SFR surface density an order of magnitude higher than *Hyde*: $\Sigma_{\text{SFR}} = 600 M_{\odot}/\text{yr}/\text{kpc}^2$.

Evidently, star-formation in *Hyde* must be less efficient than in HFLS3.

Following Daddi et al. (2010), we quantified the star-formation efficiency as $\epsilon_{\text{rot}} = \Sigma_{\text{SFR}}/(\Sigma_{\text{gas}}/t_{\text{rot}})$, where t_{rot} is the rotation period of the galaxy as derived from the $[\text{C II}]$ line kinematics (section 2.5): $t_{\text{rot}} = 8.4^{+7.9}_{-2.8} \text{ Myr}$. This leads to $\Sigma_{\text{gas}}/t_{\text{rot}} = (1.1^{+2.3}_{-0.7}) \times 10^3 M_{\odot}/\text{yr}/\text{kpc}^2$. Considering all models allowed by the SED fits, we found $\epsilon_{\text{rot}} < 0.13$ at 90% confidence. Daddi et al. (2010) observed a typical $\epsilon_{\text{rot}} \sim 0.5$ to 0.7 in our range of $\Sigma_{\text{gas}}/t_{\text{rot}}$, and our upper limit is about a factor four lower than these values. If we only consider models where *Hyde* has quenched, the upper limit on ϵ_{rot} drops to 0.01, which is more than a factor 40 below the average.

An alternative definition of the star-formation efficiency uses the free-fall time $t_{\text{ff}} = \sqrt{r_{1/2,[\text{C II}]}^3/(2G M_{\text{gas}})} = 1.2^{+0.9}_{-0.6} \text{ Myr}$. This yields upper limits of $\epsilon_{\text{ff}} < 0.023$ and 0.0019 respectively, while typical values in star-forming galaxies of similar $\Sigma_{\text{gas}}/t_{\text{ff}}$ are of the order of 0.01 (Krumholz et al. 2012). Therefore, with this definition the star-forming solutions are compatible with a standard efficiency, while quenched models are a factor five lower than normal.

4.5.2. Possible interpretations

Considering the entire parameter space allowed by the SED modeling for *Hyde*, it appears the star-formation efficiency is relatively low, at least a factor two lower than the normal value, and could be much lower if *Hyde* has recently quenched. At the same time, we have shown that the depletion time must be at least 140 Myr, and possibly larger than 1 Gyr. Since we have provided evidence in the previous sections that a recent quenching could be the correct interpretation of our observations, we need to understand how the galaxy could have quenched while keeping substantial reservoirs of inactive gas.

While quenched (or early-type) galaxies typically have very low gas fractions (e.g., Combes et al. 2007; Young et al. 2014; Sargent et al. 2015), several recent studies have reported the detection of non-star-forming gas reservoirs in quenched and post-starburst galaxies, at both low and high redshifts (e.g., Davis et al. 2014; Alatalo et al. 2014, 2015; French et al. 2015; Suess et al. 2017; Lin et al. 2017), so this is not a new concept. In particular, stacking $z \sim 2$ quiescent galaxies on sub-millimeter images, Gobat et al. (2017) found that their galaxies show a non-negligible amount of dust and gas despite their low star-formation activity. The average gas fraction they obtained ranges from $M_{\text{gas}}/M_{*} = 0.04$ to 0.13, which is substantially higher than the value for local early type galaxies, $M_{\text{gas}}/M_{*} < 0.007$.

Gobat et al. explained this low efficiency using “morphological quenching” (see Martig et al. 2009): the presence of a dense, spheroidal stellar component at the center of galaxies creates additional shear and stabilizes the gas, thus preventing star-formation. A similar interpretation was put forward in Suess et al. (2017). Given that *Hyde* has a stellar density similar to that of $z \sim 4$ quiescent galaxies (see section 4.3 and Table 1), this would be a probable scenario. The numerical simulations of Gobat et al. suggest morphological quenching should happen when the gas fraction decreases below $\sim 20\%$, which takes about 2 Gyr after the main burst in their simulation. Such long timescale seems inconsistent with a recent quenching for *Hyde*, however it is likely to vary from one galaxy to the next. The current gas fraction of *Hyde* is only constrained within $M_{\text{gas}}/(M_{\text{gas}} + M_{*}) = 12$ to 70%, so we cannot determine whether it has reached this 20% threshold or not.

Alternatively, galaxies as massive as the pair we study in this paper are expected to host super-massive black holes with masses as high as $M_{\odot} \sim 10^9 M_{\odot}$ (e.g., Reines & Volonteri 2015). These galaxies should have shone as bright quasars during the period in which their central black holes grew at a rapid rate (e.g., Trakhtenbrot et al. 2011), and the resulting radiation is believed to trigger powerful winds which can effectively quench star-formation (Silk & Rees 1998; King 2003; Cattaneo et al. 2009). If *Jekyll* and *Hyde* do host such black holes, they were not active the moment they were observed, but it is possible that *Jekyll* has experienced such a phase when it quenched, 200 to 650 Myr prior to observation.

One could also speculate that the quenching (or reduced star-formation) of *Hyde* has been caused by the feedback from its own super-massive black hole, which had stopped accreting at the time of observation; the quasar may in fact have been triggered by tidal interaction with *Jekyll*. Feedback from a central black-hole is mainly thought to act by driving powerful winds, expelling gas out of the galaxy and thus preventing it from forming stars (e.g., Silk & Rees 1998; King 2003; Faucher-Giguère & Quataert 2012; Costa et al. 2014). This scenario would not match the relatively large gas reservoir observed in *Hyde*. However, recent simulations of quasars implementing radiative transfer show that star-formation in compact high-redshift galaxies can be suppressed by radiation pressure on the dust, without removing the gas (Costa et al. in prep.). In this picture, the gas is instead redistributed in the galaxy: radiation pressure erases local over-densities, thus reducing the star formation rate, without substantially altering the gas mass or the size of the galaxy. This hypothesis could be investigated further with a more robust mapping of the gas distribution in the galaxy, for example with high-resolution CO or [C I] imaging. Deeper [C II] observations could also probe the large-scale environment and reveal whether or not gas has been expelled out of the galaxy (e.g., Ciccone et al. 2015).

In an alternative scenario, the bright quasar in *Jekyll* inhibited star-formation not only in its host galaxy, but also in *Hyde*, e.g., through radiation pressure on dust (Ishibashi & Fabian 2016). Linearly extrapolating the line-of-sight velocity of *Hyde* back in time to the point where *Jekyll* has quenched suggests both galaxies were then separated by a projected distance of 100 to 300 kpc, such that this scenario appears implausible. However, given its current separation of ~ 3 kpc, it is conceivable that a recent short quasar even in *Jekyll* indeed reduced the SFR in *Hyde*.

Finally, we note that the cessation of star-formation in *Hyde* (if any) may not be final. Given the proximity with *Jekyll*, it is possible that these galaxies have already interacted in a recent past. In this case, we could be observing *Hyde* in a temporary episode of quiescence, a few hundred Myr after an efficient burst. While the star-formation efficiency can fall below the normal value in this instance (e.g., Fensch et al. 2017), the gas density must also decrease and it is difficult to imagine it being even larger than we currently observe.

Drawing firmer conclusions would require a better measurement of the gas mass, for example using the CO(1-0) or [C I] line luminosities (e.g., Bothwell et al. 2017). A more direct measurement of the SFR, for example with H α or the Paschen series (which will be reachable with the *James Webb* Space Telescope) or high-J CO lines, would also settle the question of whether *Hyde* has truly quenched or not.

4.6. *Hyde* as a probe of *Jekyll*'s past

The constraints from our SED modeling show that *Hyde* has formed over a timescale comparable to that of *Jekyll*, but has done so at a later stage. Both galaxies are otherwise surprisingly similar: they have comparable stellar masses and sizes, and have evolved in the same environment. It is therefore tempting to regard *Hyde* as a good representation of what *Jekyll* has been shortly after (or before) having quenched. This idea is supported by the fact, demonstrated in Straatman et al. (2014), that the star-formation in the progenitors of the $z \sim 4$ quiescent galaxies must be strongly obscured, because the space density of UV-bright galaxies with the required SFRs are too low by orders of magnitude.

In this context, any conclusion we can draw on the state of *Hyde* can be translated to the progenitor of *Jekyll*, making this system a unique laboratory to study the process of quenching.

For example, if this hypothesis is true, the fact that *Hyde* may have quenched while still harboring substantial reservoirs of gas implies that *Jekyll* should also contain some amount of gas. The fraction of this gas in the molecular phase may be low, given that little on-going star-formation is presently allowed, therefore it could prove challenging to detect in CO. Tracers of atomic gas, such as [C I] or the dust continuum, may be more adequate. Currently, because the dust temperature of *Jekyll* is unknown, constraints based on the dust mass are loose. Conservatively assuming the low average temperature found by Gobat et al. (2017) in $z \sim 2$ quiescent galaxies and using the same gas-to-dust ratio as adopted in section 4.5 for *Hyde*, the non-detection of *Jekyll* in the band 8 image translates into $M_{\text{gas}} < 3.5 \times 10^{10} M_{\odot}$ (90% confidence), or a gas fraction less than 25%. This is within the range of gas fractions allowed for *Hyde*.

We finally emphasize that both galaxies were found in a cosmological survey of small area (363 arcmin^{-2}). Consequently, while *Jekyll* is among the most massive quiescent galaxies at $z \sim 4$ in this survey and may thus not be representative of the quiescent population at lower masses (see Fig. 12), it cannot be an extremely rare object either (the space density of such massive quiescent galaxies is $\sim 2 \times 10^{-5} \text{ Mpc}^{-3}$; Straatman et al. 2014). Obtaining a better understanding this pair of galaxies thus has immediate consequences for our knowledge of quenching in general.

5. Conclusions

We have obtained new and deep ALMA data towards the most distant known quiescent galaxy at $z \sim 4$ to investigate the origin of the sub-millimeter emission detected close to the line of sight. The emission was found to originate from a separate, compact source located $0.40 \pm 0.008''$ away from the quiescent galaxy on the continuum image, and spectroscopically confirmed to lie at the same redshift using the [C II] line. The line was found $549 \pm 60 \text{ km/s}$ offset from the quiescent galaxy and displays a velocity profile of a rotating disk, demonstrating it forms a separate galaxy. Careful deblending of the *Spitzer* IRAC images confirmed the presence of an additional source of near-IR emission, but no counterpart was found on the *Hubble* images, suggesting the galaxy is strongly obscured. We dubbed the quiescent and dusty galaxies *Jekyll* and *Hyde*, respectively.

Modeling of the sub-millimeter emission showed that *Hyde* has a moderate infrared luminosity, corresponding to an obscured SFR_{IR} $\sim 100 M_{\odot}/\text{yr}$. Full modeling of the UV-to-FIR emission confirmed extreme levels of obscuration of the stellar light, with $A_V \sim 3.5$, and a stellar mass comparable to its quies-

cent neighbor. This modeling further revealed that the observed dust luminosity can be fully powered by intermediate-age stars, so the current SFR may be zero, but we could not exclude that the galaxy is still forming stars on the lower envelope of the main sequence. A similar analysis of *Jekyll* confirmed its initial characterization in Glazebrook et al. (2017), its stellar mass having decreased by only 30%, and the non-detection by ALMA confirms the absence of obscured star-formation.

Fitting the kinematics of the [C II] emission of *Hyde* with a rotating disk model yielded a fast rotation period of ~ 10 Myr, a high rotation speed of ~ 700 km/s, and a compact size consistent with that of the dust continuum: $r_{1/2} = 0.67 \pm 0.14 \pm$ kpc. This size was found very similar to that of *Jekyll* ($r_{1/2} = 0.49 \pm 0.12$ kpc) and other quiescent galaxies at the same mass and redshift, suggesting *Hyde* may well be on its way to become quiescent itself.

The ratio of [C II]-to-far-IR emission in *Hyde* was found lower than any high-redshift galaxy of this luminosity. We created a toy model to determine the timescale on which the [C II]/FIR ratio can decrease following a cessation or reduction of SFR, and found that the observed ratio could be reached about 100 Myr after the end of a burst, consistent with the hypothesis that *Hyde* may have quenched.

Using various estimates of the gas mass, we showed that *Hyde* has among the highest gas surface density observed in a galaxy, rivaling that of extreme starbursts at the same redshifts. Combined with its moderate-to-low SFR and fast rotation, this implies a particularly low star-formation efficiency. Consequently, whatever phenomenon is responsible for its low star-formation activity acts more by pressurizing or stabilizing the gas, rather than depleting the reservoirs.

We finally argue that, owing to their striking similarity of compactness, environment and, perhaps, star-formation history (only shifted by ~ 400 Myr), *Jekyll* and *Hyde* can be viewed as two stages of quenching, and thus provide us with a unique laboratory to explore the physics of this poorly understood phenomenon.

A further understanding of this system could be achieved by obtaining a more direct measurement of the SFR of *Hyde*, for example using the *James Webb* Space Telescope, and constraining the gas mass of both galaxies in the three main phases: ionized (using [N II]₂₀₅), atomic (using [C I]) and molecular (using CO). Lastly, high-resolution imaging of the stellar (with *JWST*) and dust continuum (with ALMA) could reveal traces of interaction, determining if merging played an important role in shaping these galaxies.

Acknowledgements. The authors want to thank Alice Shapley for useful comments on the draft of this paper. Most of the numerical analysis conducted in this work has been performed using phy++, a free and open source C++ library for fast and robust numerical astrophysics (<http://cschreib.github.io/phypp/>). This work is based on observations taken by the CANDELS Multi-Cycle Treasury Program with the NASA/ESA *HST*, which is operated by the Association of Universities for Research in Astronomy, Inc., under NASA contract NAS5-26555. This paper makes use of the following ALMA data: ADS/JAO.ALMA#2015.A.00026.S and ADS/JAO.ALMA#2013.1.01292.S. ALMA is a partnership of ESO (representing its member states), NSF (USA) and NINS (Japan), together with NRC (Canada) and NSC and ASIAA (Taiwan) and KASI (Republic of Korea), in cooperation with the Republic of Chile. The Joint ALMA Observatory is operated by ESO, AUI/NRAO and NAOJ. G.G.K. acknowledges the support of the Australian Research Council through the award of a Future Fellowship (FT140100933).

References

Alatalo, K., Appleton, P. N., Lisenfeld, U., et al. 2014, *ApJ*, 795, 159

- Alatalo, K., Lacy, M., Lanz, L., et al. 2015, *ApJ*, 798, 31
 Allen, R. J., Kacprzak, G. G., Glazebrook, K., et al. 2017, *ApJ*, 834, L11
 Almaini, O., Wild, V., Maltby, D. T., et al. 2017, *ArXiv e-prints*, 1708.arXiv:1708.00005
 Annibali, F., Bressan, A., Rampazzo, R., et al. 2010, *A&A*, 519, A40
 Arnouts, S., Le Floch, E., Chevillard, J., et al. 2013, *A&A*, 558, 67
 Avni, Y. 1976, *ApJ*, 210, 642
 Baldry, I. K., Glazebrook, K., Brinkmann, J., et al. 2004, *ApJ*, 600, 681
 Barro, G., Faber, S. M., Pérez-González, P. G., et al. 2013, *ApJ*, 765, 104
 Bekiaris, G., Glazebrook, K., Fluke, C. J., & Abraham, R. 2016, *MNRAS*, 455, 754
 Bell, E. F., McIntosh, D. H., Katz, N., & Weinberg, M. D. 2003, *ApJS*, 149, 289
 Bendo, G. J., Baes, M., Bianchi, S., et al. 2015, *MNRAS*, 448, 135
 Bendo, G. J., Boselli, A., Dariush, A., et al. 2012, *MNRAS*, 419, 1833
 Birnboim, Y. & Dekel, A. 2003, *MNRAS*, 345, 349
 Bothwell, M. S., Aguirre, J. E., Aravena, M., et al. 2017, *MNRAS*, 466, 2825
 Brammer, G. B., van Dokkum, P. G., & Coppi, P. 2008, *ApJ*, 686, 1503
 Brisbin, D., Ferkinhoff, C., Nikola, T., et al. 2015, *ApJ*, 799, 13
 Brown, M. J. I., Moustakas, J., Smith, J. T., et al. 2014, *ApJS*, 212, 18
 Bruzual, G. & Charlot, S. 2003, *MNRAS*, 344, 1000
 Calzetti, D., Armus, L., Bohlin, R. C., et al. 2000, *ApJ*, 533, 682
 Capak, P. L., Carilli, C., Jones, G., et al. 2015, *Nature*, 522, 455
 Caputi, K. I., Ilbert, O., Laigle, C., et al. 2015, *ApJ*, 810, 73
 Cattaneo, A., Faber, S. M., Binney, J., et al. 2009, *Nature*, 460, 213
 Chabrier, G. 2003, *PASP*, 115, 763
 Charlot, S. & Fall, S. M. 2000, *ApJ*, 539, 718
 Chen, C., Smail, I., Swinbank, A. M., et al. 2015, *ApJ*, 799, 194
 Ciccone, C., Maiolino, R., Gallerani, S., et al. 2015, *A&A*, 574, A14
 Combes, F., Young, L. M., & Bureau, M. 2007, *MNRAS*, 377, 1795
 Cooky, A. L., Blake, G. A., & Saykally, R. J. 1986, *ApJ*, 305, L89
 Costa, T., Sijacki, D., & Haehnelt, M. G. 2014, *MNRAS*, 444, 2355
 Cox, P., Krips, M., Neri, R., et al. 2011, *ApJ*, 740, 63
 Croton, D. J., Springel, V., White, S. D. M., et al. 2006, *MNRAS*, 365, 11
 Croxall, K., Smith, J. D. T., Pellegrini, E., et al. 2017, *ArXiv e-prints*, 1707.arXiv:1707.04435
 da Cunha, E., Charlot, S., & Elbaz, D. 2008, *MNRAS*, 388, 1595
 da Cunha, E., Walter, F., Smail, I. R., et al. 2015, *ApJ*, 806, 110
 Daddi, E., Dannerbauer, H., Krips, M., et al. 2009a, *ApJ*, 695, L176
 Daddi, E., Dannerbauer, H., Stern, D., et al. 2009b, *ApJ*, 694, 1517
 Daddi, E., Elbaz, D., Walter, F., et al. 2010, *ApJ*, 714, L118
 Davé, R., Thompson, R., & Hopkins, P. F. 2016, *MNRAS*, 462, 3265
 Davis, T. A., Young, L. M., Crocker, A. F., et al. 2014, *MNRAS*, 444, 3427
 De Breuck, C., Maiolino, R., Caselli, P., et al. 2011, *A&A*, 530, L8
 Diaz-Santos, T., Armus, L., Charmandaris, V., et al. 2017, *ArXiv e-prints*, 1705.arXiv:1705.04326
 Draine, B. T. & Li, A. 2007, *ApJ*, 657, 810
 Dunlop, J. S., McLure, R. J., Biggs, A. D., et al. 2017, *MNRAS*, 466, 861
 Díaz-Santos, T., Armus, L., Charmandaris, V., et al. 2013, *ApJ*, 774, 68
 Elbaz, D., Dickinson, M., Hwang, H. S., et al. 2011, *A&A*, 533, 119
 Erwin, P. 2015, *ApJ*, 799, 226
 Eufrazio, R. T., Lehmer, B. D., Zezas, A., et al. 2017, *ArXiv e-prints*, 1710.arXiv:1710.09401
 Faucher-Giguère, C. & Quataert, E. 2012, *MNRAS*, 425, 605
 Fensch, J., Renaud, F., Bournaud, F., et al. 2017, *MNRAS*, 465, 1934
 Förster Schreiber, N. M., Genzel, R., Newman, S. F., et al. 2014, *ApJ*, 787, 38
 Franx, M., Labbé, I., Rudnick, G., et al. 2003, *ApJ*, 587, L79
 French, K. D., Yang, Y., Zabludoff, A., et al. 2015, *ApJ*, 801, 1
 Gabor, J. M. & Davé, R. 2012, *MNRAS*, 427, 1816
 Galliano, F., Hony, S., Bernard, J., et al. 2011, *A&A*, 536, A88
 Genzel, R., Förster Schreiber, N. M., Rosario, D., et al. 2014, *ApJ*, 796, 7
 Glazebrook, K., Abraham, R. G., McCarthy, P. J., et al. 2004, *Nature*, 430, 181
 Glazebrook, K., Schreiber, C., Labbé, I., et al. 2017, *Nature*, 544, 71
 Gobat, R., Daddi, E., Magdis, G., et al. 2017, *ArXiv e-prints*, 1703.arXiv:1703.02207
 Gobat, R., Strazzullo, V., Daddi, E., et al. 2012, *ApJ*, 759, L44
 Gullberg, B., De Breuck, C., Vieira, J. D., et al. 2015, *MNRAS*, 449, 2883
 Guo, Y., Giavalisco, M., Ferguson, H. C., Cassata, P., & Koekemoer, A. M. 2012, *ApJ*, 757, 120
 Hodge, J. A., Swinbank, A. M., Simpson, J. M., et al. 2016, *ApJ*, 833, 103
 Huang, J., Zheng, X. Z., Rigopoulou, D., et al. 2011, *ApJ*, 742, L13
 Ilbert, O., McCracken, H. J., Le Fèvre, O., et al. 2013, *A&A*, 556, 55
 Ishibashi, W. & Fabian, A. C. 2016, *MNRAS*, 457, 2864
 Kapala, M. J., Groves, B., Sandstrom, K., et al. 2017, *ApJ*, 842, 128
 Kennicutt, Robert C., J. 1998, *ARA&A*, 36, 189
 King, A. 2003, *ApJ*, 596, L27
 Koekemoer, A. M., Aussel, H., Calzetti, D., et al. 2007, *ApJS*, 172, 196
 Kriek, M., van Dokkum, P. G., Labbé, I., et al. 2009, *ApJ*, 700, 221
 Krumholz, M. R., Dekel, A., & McKee, C. F. 2012, *ApJ*, 745, 69
 Labbé, I., Franx, M., Rudnick, G., et al. 2007, *ApJ*, 665, 944
 Labbé, I., Oesch, P. A., Illingworth, G. D., et al. 2015, *ApJS*, 221, 23
 Lapham, R. C., Young, L. M., & Crocker, A. 2017, *ApJ*, 840, 51

Lee, J. H., Lee, M. G., Park, C., & Choi, Y. 2010, MNRAS, 403, 1930
 Leroy, A. K., Bolatto, A., Gordon, K., et al. 2011, ApJ, 737, 12
 Lin, L., Belfiore, F., Pan, H., et al. 2017, ArXiv e-prints, 1710.08610
 Luhman, M. L., Satyapal, S., Fischer, J., et al. 1998, ApJ, 504, L11
 Lutz, D., Berta, S., Contursi, A., et al. 2016, A&A, 591, A136
 Madau, P. & Dickinson, M. 2014, ARA&A, 52, 415
 Madden, S. C., Geis, N., Genzel, R., et al. 1993, ApJ, 407, 579
 Malhotra, S., Helou, G., Stacey, G., et al. 1997, ApJ, 491, L27
 Malhotra, S., Kaufman, M. J., Hollenbach, D., et al. 2001, ApJ, 561, 766
 Martig, M., Bournaud, F., Teyssier, R., & Dekel, A. 2009, ApJ, 707, 250
 Martí-Vidal, I., Vlemmings, W. H. T., Muller, S., & Casey, S. 2014, A&A, 563, A136
 Muzzin, A., Marchesini, D., Stefanon, M., et al. 2013, ApJ, 777, 18
 Nakagawa, T., Doi, Y., Yui, Y. Y., et al. 1995, ApJ, 455, L35
 Nanayakkara, T., Glazebrook, K., Kacprzak, G. G., et al. 2016, ApJ, 828, 21
 Noll, S., Burgarella, D., Giovannoli, E., et al. 2009, A&A, 507, 1793
 Oteo, I., Ivison, R. J., Dunne, L., et al. 2016, ApJ, 827, 34
 Papovich, C., Dickinson, M., & Ferguson, H. C. 2001, ApJ, 559, 620
 Pasquali, A., Ferreras, I., Panagia, N., et al. 2006, ApJ, 636, 115
 Peng, C. Y., Ho, L. C., Impey, C. D., & Rix, H. 2002, AJ, 124, 266
 Peng, Y., Maiolino, R., & Cochrane, R. 2015, Nature, 521, 192
 Peng, Y.-j., Lilly, S. J., Kovač, K., et al. 2010, ApJ, 721, 193
 Poggianti, B. M. & Wu, H. 2000, ApJ, 529, 157
 Qin, Y., Mutch, S. J., Duffy, A. R., et al. 2017, arXiv:1704.03274 [astro-ph]
 Reddy, N. A., Pettini, M., Steidel, C. C., et al. 2012, ApJ, 754, 25
 Reines, A. E. & Volonteri, M. 2015, ApJ, 813, 82
 Riechers, D. A., Bradford, C. M., Clements, D. L., et al. 2013, Nature, 496, 329
 Riechers, D. A., Carilli, C. L., Capak, P. L., et al. 2014, ApJ, 796, 84
 Rong, Y., Jing, Y., Gao, L., et al. 2017, MNRAS, 471, L36
 Rujopakarn, W., Dunlop, J. S., Rieke, G. H., et al. 2016, ApJ, 833, 12
 Saintonge, A., Catinella, B., Cortese, L., et al. 2016, MNRAS, 462, 1749
 Sargent, M. T., Daddi, E., Bournaud, F., et al. 2015, ApJ, 806, L20
 Schaerer, D., Boone, F., Jones, T., et al. 2015, A&A, 576, L2
 Schreiber, C., Elbaz, D., Pannella, M., et al. 2016, A&A, 589, A35
 Schreiber, C., Elbaz, D., Pannella, M., et al. 2017a, A&A, 602, A96
 Schreiber, C., Labbé, I., Glazebrook, K., et al. 2017b, ArXiv e-prints, 1709.arXiv:1709.03505
 Schreiber, C., Pannella, M., Elbaz, D., et al. 2015, A&A, 575, A74
 Silk, J. & Rees, M. J. 1998, A&A, 331, L1
 Simpson, J. M., Smail, I., Wang, W., et al. 2017, ApJ, 844, L10
 Sklias, P., Schaerer, D., Elbaz, D., et al. 2017, ArXiv e-prints, 1705.arXiv:1705.01174
 Sklias, P., Zamojski, M., Schaerer, D., et al. 2014, A&A, 561, 149
 Smit, R., Bouwens, R. J., Carniani, S., et al. 2017, arXiv:1706.04614 [astro-ph]
 Smith, J. D. T., Croxall, K., Draine, B., et al. 2017, ApJ, 834, 5
 Smolčić, V., Delvecchio, I., Zamorani, G., et al. 2017, A&A, 602, A2
 Stacey, G. J., Geis, N., Genzel, R., et al. 1991, ApJ, 373, 423
 Stacey, G. J., Hailey-Dunsheth, S., Ferkinhoff, C., et al. 2010, ApJ, 724, 957
 Stark, D. P., Schenker, M. A., Ellis, R., et al. 2013, ApJ, 763, 129
 Straatman, C. M. S., Labbé, I., Spitler, L. R., et al. 2014, ApJ, 783, L14
 Straatman, C. M. S., Labbé, I., Spitler, L. R., et al. 2015, ApJ, 808, L29
 Straatman, C. M. S., Spitler, L. R., Quadri, R. F., et al. 2016, ApJ, 830, 51
 Suess, K. A., Bezanson, R., Spilker, J. S., et al. 2017, ArXiv e-prints, 1708.arXiv:1708.03337
 Swinbank, A. M., Karim, A., Smail, I., et al. 2012, MNRAS, 427, 1066
 Swinbank, A. M., Papadopoulos, P. P., Cox, P., et al. 2011, ApJ, 742, 11
 Tan, Q., Daddi, E., Magdis, G., et al. 2014, A&A, 569, A98
 Targett, T. A., Dunlop, J. S., Cirasuolo, M., et al. 2013, MNRAS, 432, 2012
 Tielens, A. G. G. M. & Hollenbach, D. 1985, ApJ, 291, 722
 Tomczak, A. R., Quadri, R. F., Tran, K. H., et al. 2014, ApJ, 783, 85
 Trakhtenbrot, B., Lira, P., Netzer, H., et al. 2017, ApJ, 836, 8
 Trakhtenbrot, B., Netzer, H., Lira, P., & Shemmer, O. 2011, ApJ, 730, 7
 Valtchanov, I., Virdee, J., Ivison, R. J., et al. 2011, MNRAS, 415, 3473
 Venemans, B. P., Walter, F., Zschaechner, L., et al. 2016, ApJ, 816, 37
 Wagg, J., Wiklind, T., Carilli, C. L., et al. 2012, ApJ, 752, L30
 Walter, F., Decarli, R., Carilli, C., et al. 2012, Nature, 486, 233
 Wang, T., Elbaz, D., Schreiber, C., et al. 2016, ApJ, 816, 84
 Weingartner, J. C. & Draine, B. T. 2001, ApJS, 134, 263
 Wellons, S., Torrey, P., Ma, C., et al. 2015, MNRAS, 449, 361
 Wilkinson, C. L., Pimbblet, K. A., & Stott, J. P. 2017, ArXiv e-prints, 1708.arXiv:1708.03168
 Williams, R. J., Quadri, R. F., Franx, M., van Dokkum, P., & Labbé, I. 2009, ApJ, 691, 1879
 Wu, H., Zou, Z. L., Xia, X. Y., & Deng, Z. G. 1998, A&AS, 132, 181
 Young, L. M., Scott, N., Serra, P., et al. 2014, MNRAS, 444, 3408

Appendix A: Simulated star-formation histories

The family of star-formation histories generated by Eq. 1 allows for a wide variety of scenarios, but is nevertheless simplistic. In reality, star-formation histories could be less smooth, and composed of multiple bursts. To explore whether our model still provides meaningful results in these scenario, we have generated a suite of 400 simulated galaxies with more complex SFHs. These SFHs were created as the sum of N bursts of variable peak intensity (SFR_b) and duration (τ_b), each burst being arbitrarily modeled as a Gaussian. The motivation for the latter is to avoid, on purpose, a functional form too similar to that assumed by Eq. 1, in order to test how our model behaves when the true SFH has no perfect match in the grid. The time at which each burst happened (t_b) was drawn from a Gaussian distribution centered on a “main burst” time (t_{main}) and with a given “main burst length” width (τ_{main}); t_{main} itself was drawn uniformly between the Big Bang and the epoch of observation, and τ_{main} was drawn uniformly between 10 and 500 Myr. The number of bursts was chosen randomly from $N = 1$ to $100 \times (\tau_{\text{main}} - 10)/490$ (with uniform probability in $\log N$) and the length of each burst was chosen randomly from $\tau_b = 10$ to 200 Myr (with uniform probability in $\log \tau_b$). These values were chosen so as to provide a full coverage of the $t_{b<1\%} - t_{68\%}$ plane (i.e., Fig. 10).

We then used the Bruzual & Charlot (2003) stellar population models to create the corresponding SED for each simulated SFH, and generated two photometric catalogs based on these SEDs: one with $A_V = 0.5$ mag, as observed for *Jekyll*, and another with 3.5 mag, as observed for *Hyde*. In the first catalog the SEDs were normalized to match *Jekyll*’s K_s -band flux, while in the second catalog the SEDs were normalized to match *Hyde*’s $4.5 \mu\text{m}$ flux. The flux uncertainties were chosen to be the same as observed for *Jekyll* and *Hyde*, respectively.

We then ran FAST++ on these simulated SEDs with the same setup as for *Jekyll* and *Hyde*, i.e., using the model SFH of Eq. 1 (the only difference being that the simulations did not include the MOSFIRE spectrum, for simplicity). We then defined the region of the $t_{b<1\%} - t_{68\%}$ plane allowed within $\Delta\chi^2 < 2.71$ and determined, for each simulated galaxy, if the true value of $t_{b<1\%}$ and $t_{68\%}$ actually fell inside this region.

We found that 90% and 95% of the simulated SFHs were correctly recovered for $A_V = 0.5$ and 3.5 mag, respectively, which shows that our simplistic model is indeed able to account for more complex SFHs than that of Eq. 1. Examples of galaxies properly recovered by our model despite their complex SFH are shown on the first row of Fig. A.1 and A.2.

Since the percentages above are only representative of our simulated data set and not of real star-formation histories, it is illuminating to look at the few cases where the model clearly failed. We show on the second and third rows of Fig. A.1 and A.2 selected examples which illustrate the most major deficiencies. In all these cases, the SFH can be described as being composed of two distinct bursts separated by a few hundreds Myr of quiescence.

For *Jekyll*-like galaxies (Fig. A.1), we observe two different types of problems. In the first case (second row on the figure), the true SFH is composed of two main star-formation episodes, the first being very old ($t_{\text{obs}} - t > 1000$ Myr), and the second more recent (200 Myr). The entire SFH is poorly recovered; the model tries to account for both bursts and thus obtains twice longer formation timescales compared to the true SFH. Doing so, it even fails at recovering the fully quiescent nature of the galaxy (in terms of $t_{b<1\%}$; the estimated current SFR is still fairly low). However it is also clear that the adopted model is a poor fit

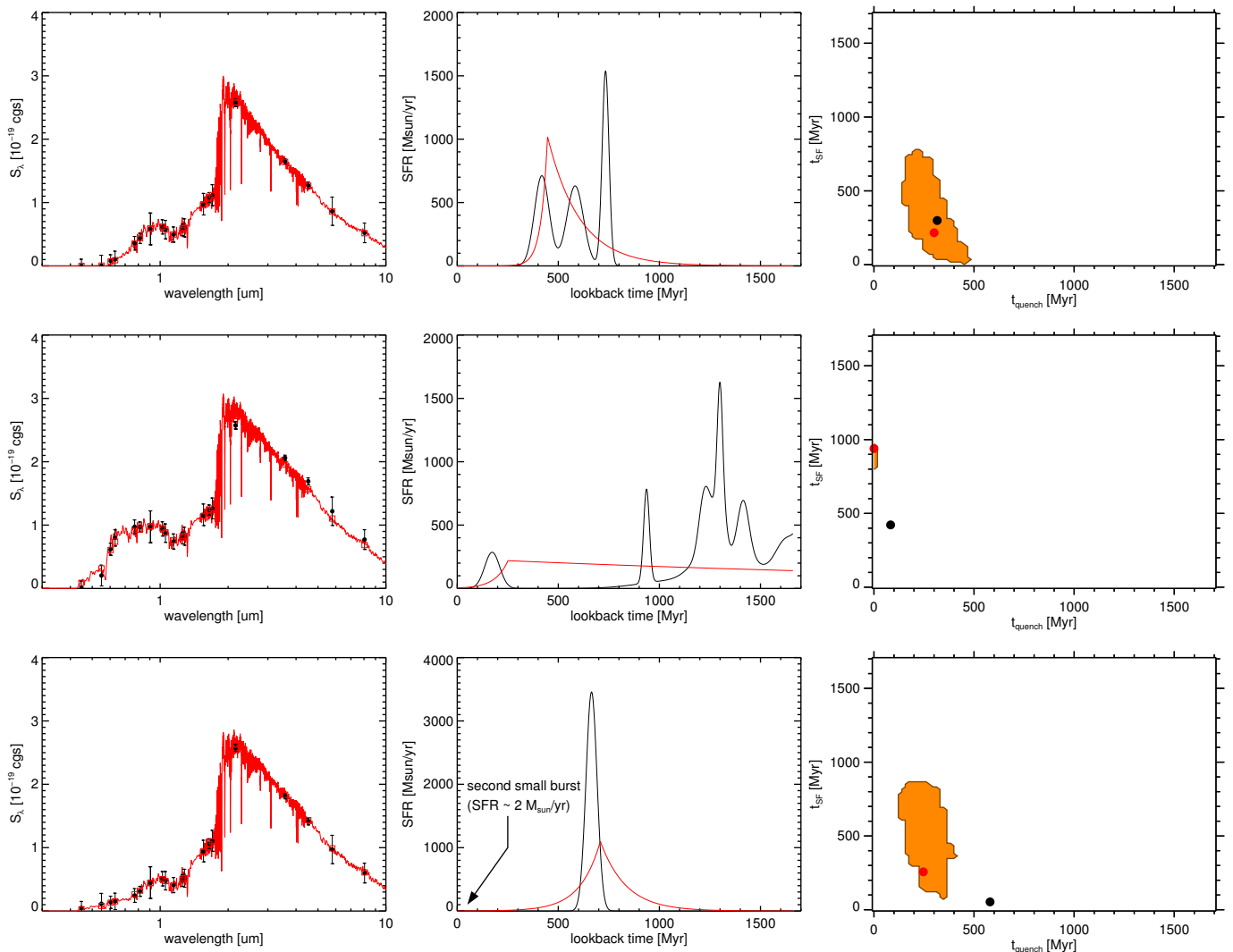


Fig. A.1. Simulated star-formation histories for comparison with *Jekyll*. The first row shows a quenched star-formation history composed of three bursts. The second row shows an SFH where most of the mass was formed very early, and a small burst happened 200 Myr before observation, creating the post-starburst features. The third row shows an SFH with two bursts, the last one happening when the galaxy is observed but has a very small SFR. **Left:** synthetic photometry for the complex SFH (black points) and best-fit model from FAST++ (red line and red squares). **Middle:** complex star-formation history (black) and best-fit model (red). **Right:** constraints on the formation and quenching timescales ($t_{68\%}$ and $t_{b<1\%}$) given by the model (orange area), best-fit value (red circle) and true value (black circle).

to the photometry: the observed K_s and *Spitzer* bands are off by more than 2σ . Such cases, if they happen, would be identifiable easily.

The second case is more subtle. The true SFH in this case is also composed of two bursts, the first is moderately old ($t_{\text{obs}} - t \sim 700$ Myr) but the second has extremely small SFR and is still on-going at the time of observation. The peak SFR of this second burst is only $2 M_{\odot}/\text{yr}$, compared to several thousands for the main burst. The photometry is therefore dominated by the older burst, where most of the stars formed, but one can see that the on-going star-formation also leaves a noticeable trace in the UV. The model is forced to account for the main component, but it also tries to reproduce the small residual SFR coming from the second burst by using a long e -folding timescale for the post-burst decline. This results in a shorter quiescent time than that of the true SFH, and implies that our quenching times could be biased toward shorter values.

For *Hyde*-like galaxies (Fig. A.2), we found similarly problematic SFHs. However, because the photometry there is glob-

ally of poorer S/N , the most stringent constraint is actually coming from the observed L_{IR} . This results in a different impact on the derived parameters. Essentially, if an older burst is present in the true SFH, it is mostly ignored by the model and the most recent burst is fairly well described. In the first case illustrated on Fig. A.2 (second row), the formation timescale is enlarged to accommodate the older burst, but the quenching time is correctly captured. In the second case, the late burst happens at the epoch of observation and thus totally dominates the L_{IR} ; the oldest burst is completely ignored. The recovered stellar mass is a factor two lower than its true value. This is commonly referred to as the “outshining” phenomenon (Papovich et al. 2001), and implies that there may have been more star-formation happening at earlier epochs in *Hyde* compared to what our model suggests. We emphasize that outshining is only a problem when our model SFH cannot reproduce the true SFH. In other cases, the only impact of outshining is to enlarge error bars on model parameters (in particular on the stellar mass).

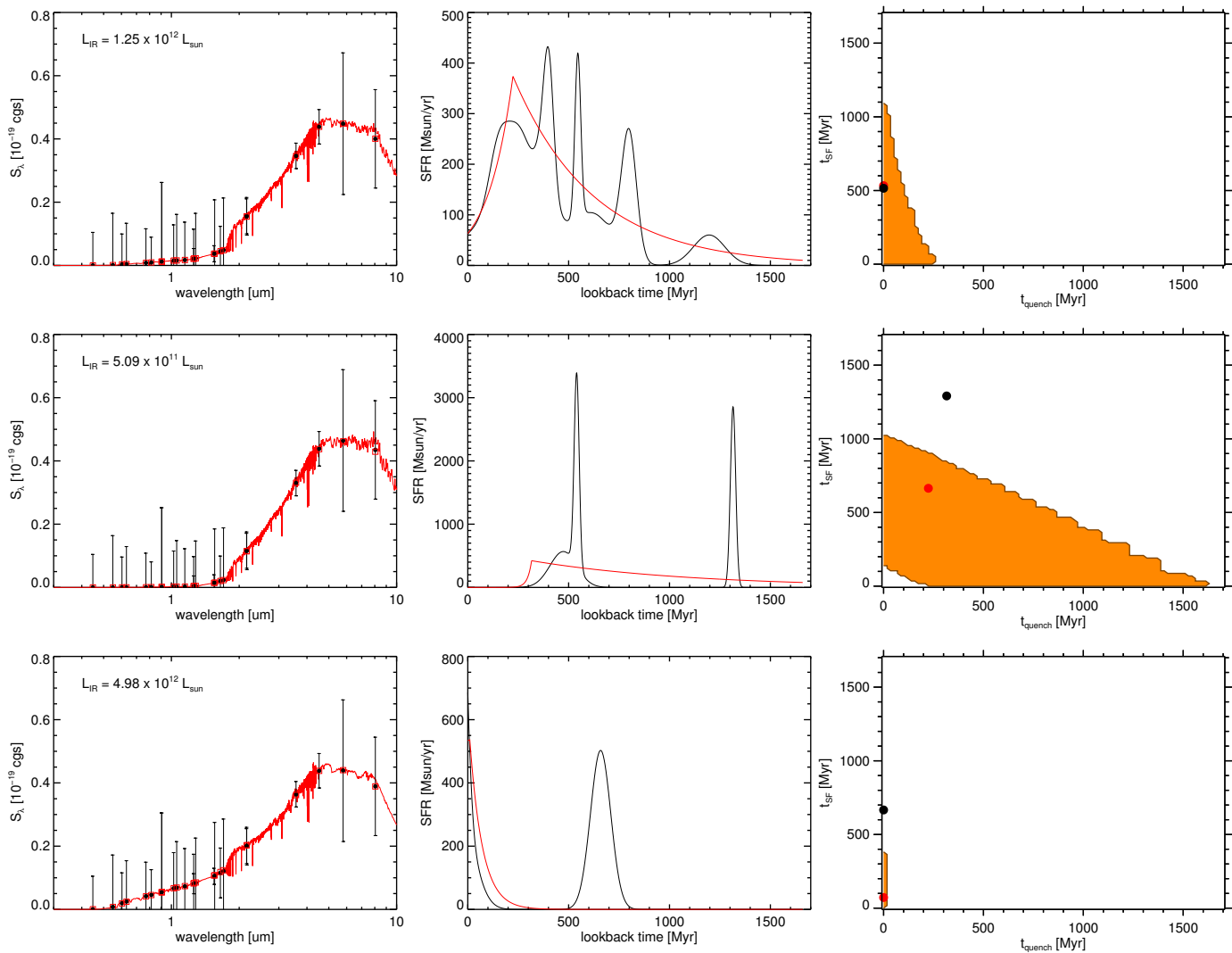


Fig. A.2. Same as Fig. A.2, but for comparison with *Hyde*. On the left column we also give the model's L_{IR} (since the SEDs are otherwise very similar). The first row shows a star-formation history which lasts steadily for several hundred million years but is composed of multiple bursts and dips, then slowly fades out 200 Myr before the observation. The second row shows an SFH with essentially two bursts happening at least 500 Myr prior observation. The third row shows an SFH with two burst, the last one happening when the galaxy is observed.